Summer 8-2-2012

Characterization of Magnetic Nanostructured Materials by First Order Reversal Curve Method

Denny R. Lenormand
University of New Orleans, dlenorma@uno.edu

Characterization of Magnetic Nanostructured Materials by First Order Reversal Curve Method

A Thesis

Submitted to the Graduate Faculty of the
University of New Orleans
in partial fulfillment of the
requirements for the degree of

Master of Science
in
Applied Physics

by

Denny Lenormand

B.S University of New Orleans, 2010

August 2012

Acknowledgements

First and foremost, I would like to thank Professor Leonard Spinu for accepting me into his research group. His guidance has made my journey through graduate school rewarding. His understanding and passion for physics, nanomagnetism in particular, creates an ideal learning environment for students and upcoming physicists.

I would like to extend a thank you to the Advanced Materials Research Institute (AMRI) and Louisiana Board of Regents Contract #LEQSF(2007-12)-ENH-PKSFI-PRS-04 for all the financial support throughout my undergraduate and graduate careers.

The University of New Orleans Physics staff have become like a family to me. I would like to thank the entire physics staff for putting up with my shenanigans for 5 long years.

Big thank you to Professor Kevin Stokes for helping me through a slight melt down while I was taking a course in E&M using the Jackson book.

Thank you to Dr. Jose Vargas for pushing me to complete variousprojects..

Thank you to all the guys I grapple and train with. Training was the one thing that kept me sane the last two years.

To my lab mate and friend Andrei Diaconu, being my peer, his view on magnetism has helped my understanding vastly. Thanks.

I would like to thank Prof. John Wiley (UNO, Chemistry) and Dr. Ganping Ju (Seagate)for providing me with the samples included in this research.

Thank you Dr. Juliet Ioup for editing this thesis

Lastly, I would like to thank my thesis committee, Professor Leonard Spinu, Professor Kevin Stokes, and Professor Leszek Malkinski for taking the time and energy to review my work.

Table of Contents

List of Figures

List of Tables

Abstract

The Interactions and magnetization reversal of Ni nanowire arrays and synthetic anit-ferromagnetic coupled thin film trilayers have been investigated through first order reversal curve (FORC) method. By using a quantitative analysis of the local interaction field profile distributions obtained from FORC, it has proven to be a powerful characterization tool that can reveal subtle features of magnetic interactions.

First Order Reversal Curve, Nanowires, Synthetic Anti-Ferromagnets, Magnetization Reversal

Introduction

Magnetic materials have evolved from being a magical stone to one of the most commonly used material. Present day technology revolves around magnets, ferromagnets to be specific. Ferromagnets and being the most common known, yet by far are the most interesting and complex.

The applications of ferromagnetic material in information storage devices, such as computers, cell phone, and nonolatile memory have caused them to be much desired. As technology progresses forward so does the desire for more efficient materials. Present day technology cause for information storage devices to be convenient enough to carry around in a pocket. Hence, sizes matters.

Magnetic nanostructured materials, whereas their components have at least one dimension below 100 nm, are important to both theoretical and experimental studies. Magnetic nanowires, i.e. materials with two dimensions at nanometer scale, in particular are commonly studied as an array of nanowires fabricated by depositing magnetic material into a nanoporous template. Materials such as track-etched polymers and anodic porous alumina allow for uniform control of nanowires. Consequently, the interaction properties of the magnetic nanowires greatly depend on the quality of the template used. This thesis will focus on the study of magnetic nanowires in templates obtained by aluminum anodization.

In the study ferromagnetic materials the main feature that stands out is the major hysteresis loop. Although the major hysteresis loop gives some information, it has proven to be inadequate in producing information about the interactions within a magnetic system. The first order reversal curve (FORC) method probes the interior of the major hysteresis loop and it was

shown that has the ability to reveal the interactions within the system. After it was introduced by Mayergoyz, the first order reversal curve method soon became a protocol in characterize various ferromagnetic material systems [1]. This thesis will focus on the characterization of nanostructured materials using the first order reversal curve method.

The following is an outline of this thesis:

Chapter 1: *A Brief Introduction into Magnetism.* This chapter gives an overview of the concepts in magnetism that are crucial in the understanding of the content of this thesis. The background information includes magnetic free energy, insight into magnetic domains, an overview of the Stoner-Wohlfarth, Neel-Brown, and classical Preisach models.

Chapter 2: *Experimental Techniques.* This chapter gives an overview of the experimental techniques used in the research throughout this thesis. The content includes obtaining magnetization curves such as the major hysteresis loops and first order reversal curves (FORC), the program used to process the FORCs, the synthesis processes of the materials used, and the magnetometers used to characterize the materials.

Chapter 3: *Interactions and Field Reversal Memory in Complex Nanowire Arrays.* In this chapter the interaction and magnetic reversal behavior in a series of 12 Ni nanowire arrays, of different configurations are quantitatively analyzed using first order reversal curve method.

Chapter 4: *Mapping internal fields and interactions on synthetic antiferromagnetic materials by FORC analysis: FeCoB/Ru/FeCoB trilayers.* This chapter is a FORC study of synthetic antiferromagnetic materials.

Chapter 5: *Conclusions.* This chapter gives the conclusion in this thesis.

Chapter 1: A Brief Introduction to Magnetism

1.1 *Introduction*

In this chapter the main theoretical concepts necessary for describing the research work in this thesis. Specifically, the contribution to the magnetic free energy and overview of some basic models describing the static and dynamic properties of magnetization will be reviewed.

1.2 *Magnetic Energy*

1.2.1 *Magnetic anisotropy*

The magnetic behavior of materials is greatly dependent on factors such as their crystal structure, shape, and the effects of stresses. All of these can be grouped together as magnetic anisotropy. Magnetic anisotropy plays an important role in the shape of the magnetization curves such as the major hysteresis loop (MHL). The MHL is one of the main characteristics of magnetic material and will be explained in some detail in a later chapter. The measured magnetic properties in a given system can yield dramatically different results depending on the direction of the applied magnetic field $\boldsymbol{H}$ with respect to the specimen. Thus, the magnetic anisotropy will alter the outcome of the magnetization curves and is one of the most important properties of magnetic materials. In the following will be mentioned the main contributions to magnetic anisotropy.

1.2.1.1 *Magnetocrystalline anisotropy*

Magnetocrystalline anisotropy can be considered as an intrinsic property of ferromagnetic materials. The origin of magnetocrystalline anisotropy can be associated partially with the exchange interaction between two neighboring spins. The exchange interaction can be explained as spin-spin coupling between neighboring electrons. Spin-spin coupling is a strong and important interaction which will be explained in more detail in later sections. However, the exchange interaction between spins is only part of the story. For example, as an external field $\boldsymbol{H}$ is applied in an attempt to reorient the spins the orbitals associated with the spins are also reoriented[2]. The orbitals resist the reorientation due to applied field $\boldsymbol{H}$ because of their strong coupling with the crystal lattice, giving rise to a preferred direction of magnetization. The applied field $\boldsymbol{H}$ reorients the spins, which are coupled to the orbital, which are strongly coupled to the lattice, which consequently have a tendency to resist movement. This is known as spin-orbit coupling. Also, the energy it takes to pull the magnetic moments away from the preferred axis of magnetization is the anisotropy energy. The preferred axis of magnetization is known as the easy axis (*EA*) of magnetization. The anisotropy energy is at a minimum on the *EA*. Consider a hexagonal crystal lattice with uniaxal anisotropy such as cobalt (Co) with a single angle θ between the $\boldsymbol{M}_s$ vector and the long axis. The energy density can be written as,

$$E_K = K_o + K_1 sin^2\theta + K_2 sin^4\theta + \cdots, \tag{1.1}$$

where θ is the angle the magnetization $\boldsymbol{M}$ makes with the c-axis and K_n *(n=0, 1, 2, 3…)* are the anisotropy constants. For Co K_o is a constant and K_2 and higher order terms are very small so they can be neglected. The energy density can be written such that

$$E_K = K_1 sin^2\theta \tag{1.2}$$

For cubic crystals such as iron (Fe) and nickel (Ni), the energy density can be written in terms of direction cosines such that,

$$E_k = K_1(\alpha_1^2\alpha_2^2 + \alpha_2^2\alpha_3^2 + \alpha_3^2\alpha_1^2) + K_2\alpha_1^2\alpha_2^2\alpha_3^2 + \cdots \quad (1.3)$$

where (α_1, α_2, α_3) are the direction cosines of the magnetization vector with respect to the cubic axes.

1.2.1.2 *Shape anisotropy*

The shape of the magnetic specimen will affect the outcome of the magnetization measurements and resultant curves. As an external magnetic field $\boldsymbol{H}$ is applied an accumulation of free poles emerges on the ends of the specimen producing an oppositional field to the direction of magnetization [3]. This opposing field is known as the demagnetization field and can be written as

$$\boldsymbol{H}_d = -N\boldsymbol{M}, \quad (1.4)$$

where N is the demagnetization factor dependent solely on the geometry of a given specimen[4].

The energy of the demagnetizing field is called magnetostatic energy [2]. The magnetostatic energy density can be written as follows

$$E_D = \frac{1}{2}\boldsymbol{H}_d \cdot \boldsymbol{M}, \quad (1.5)$$

where $\boldsymbol{H}_d$ is the associated demagnetizing field produced by specimen's particular geometry.

Now let us consider a prolate ellipsoid magnetized at an arbitrary magnetization $\boldsymbol{M}$ at an angle θ, as shown in figure 1.1.

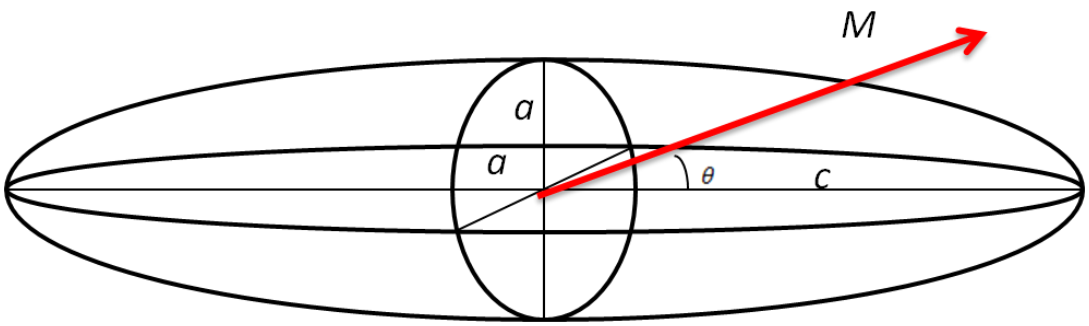

Figure 1.1: A Schematic of a prolate sphere.

The magnetostatic energy density E_D for a prolate ellipsoid with minor axes *a and b*, major axis *c*, and where $a=b < c$, can be written as

$$E_D = \frac{1}{2}[(Mcos\theta)^2 N_c + (Msin\theta)^2 N_a]\,, \tag{1.6}$$

where $N_a = N_b$, and N_c are the demagnetizing factors associated with the three principal axes of the prolate ellipsoid *a*, *b*, and *c*, respectively, and $N_a + N_b + N_c = 4\pi$. The demagnetizing factors for a prolate ellipsoid can be written as

$$N_c = \frac{C_3}{(m^2-1)}\left[\frac{m}{\sqrt{m^2-1}}\ln\left(m+\sqrt{m^2-1}\right)-1\right] \tag{1.7}$$

and

$$N_a = N_b = \frac{C_3 - N_c}{2}\,, \tag{1.8}$$

where $C_3 = 4\pi$ and the aspect ratio $m = c/a$. As m becomes large the demagnetizing factors take the form

$$N_c \approx \frac{C_3}{m^2}(\ln(2m)-1) \tag{1.9}$$

$$N_a = N_b \approx \frac{C_3}{2}. \tag{1.10}$$

Substituting $cos^2\theta = 1 - sin^2\theta$ into equation (1.5) we obtain

$$E_D = \frac{1}{2}M^2N_c + \frac{1}{2}(N_a - N_c)M^2sin^2\theta \tag{1.11}$$

The angular dependence of the magnetostatic energy has a similar form to that of the uniaxial crystal anisotropy energy given in equation (1.2) [2]. The shape anisotropy constant K_s can be written as

$$K_s = \frac{1}{2}(N_a - N_c)M^2. \tag{1.12}$$

Consequently, the long axis of a given specimen adopts the role of the easy axis (uniaxial crystals). As the aspect ratio increases the anisotropy constant K_s increases and the demagnetizing factor decreases along the long axis. We also find in the case of a sphere where $a = c$ and $N_a = N_c$ the shape anisotropy vanishes.

The magnetic properties and domain behavior of complex nanostructures such as magnetic nanowires arrays depend on the magnetostatic energy as we will see in later sections.

1.2.1.3 *Magnetostriction and stress anisotropy*

When an external field ***H*** is applied to a given specimen, its dimensions change (figure 1.2). This phenomenon is known as magnetostriction. This dimensional change can be expressed as a strain λ

$$\lambda = \frac{\Delta l}{l}, \tag{1.13}$$

where λ is the magnetically induced strain on the system, and $\Delta l/l$ is the fractional change in length. The strain of a system can be positive or negative depending on the material used. Magnetostriction is caused mainly by spin-orbit coupling [2]. As mentioned in section 1.2.1.1 spin-orbit coupling is also responsible for magnetocrystalline anisotropy. As an applied field attempts to reorient the magnetic moments of a given system, the associated orbits are reoriented causing a deformation of the domains. Each domain being deformed results in a total deformation of the specimen as a whole. When a specimen has reached the saturation magnetization the value of λ reaches saturation as well, this term is known as saturation magnetostriction.

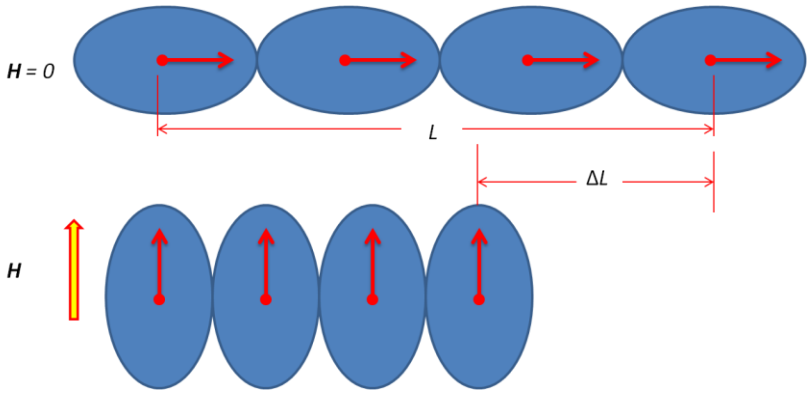

Figure 1.2: Example of magnetostiction. The example depicts an enormous strain. In general, the change is very small.

Consider the magnetization when a specimen is under tensile stress figure 1.3a and/or compressive stress Figure 1.3(b). The application of an external stress can alter the domain structure giving rise to a source of magnetic anisotropy or stress anisotropy and induces an EA of magnetization.

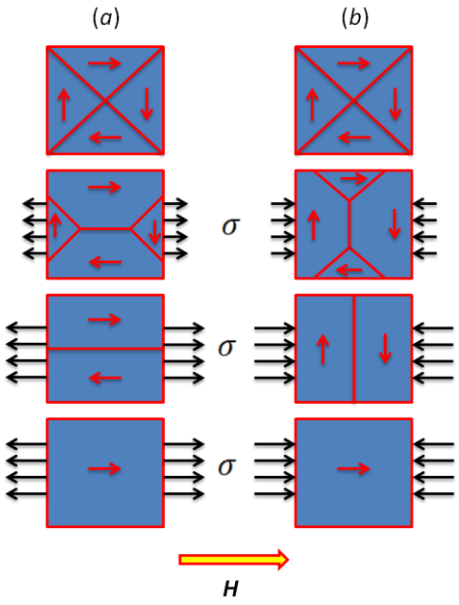

Figure 1.3: (a) Magnetization processes in a material with a positive magnetostriction under a tensile stress. (b) Magnetization processes in a material with a positive magnetostriction under a compressive stress.

The energy density of a system experiencing stress is called magnetoelastic energy E_{me} written as

$$E_{me} = \frac{3}{2}\lambda_{si}\sigma sin^2\theta, \tag{1.14}$$

where λ_{si} is the magnetotstriction, σ is the induced stress, and θ is the angle between the magnetization $\boldsymbol{M}$ and the stress σ. The magnetoelastic energy can also be written as

$$E_{me} = K_\sigma sin^2\theta \tag{1.15}$$

where K_σ is the stress anisotropy constant equal to $\frac{3}{2}\lambda_{si}\sigma$ for a system that exhibits isotropic magnetostrictive behavior.

1.2.2 *Zeeman Energy*

Interactions between the external applied field $\boldsymbol{H}$ and the magnetization vector $\boldsymbol{M}$ produce a free energy term known as the Zeeman energy. The Zeeman energy density E_Z can be written as the negative of the dot product of the two vectors

$$E_Z = -\boldsymbol{M} * \boldsymbol{H} \tag{1.16}$$

where $\boldsymbol{M}$ is the magnetization vector and $\boldsymbol{H}$ is the applied field.

1.2.3 *Exchange Energy*

The spins of electrons in magnetic materials experience a strong coupling (spin-spin) known as exchange interaction. While the exchange interaction is a strong interaction, it diminishes quickly with distance. It can be considered as a short range interaction and simplified by limiting the summation to neighboring spins. The exchange energy term can be written as

$$E_{ex} = -2\sum_{ij} J_{ij}\, \boldsymbol{S}_i \boldsymbol{S}_j, \tag{1.17}$$

where $\boldsymbol{S}_i$ and $\boldsymbol{S}_j$ are the moment vectors and J_{ex} is the exchange integral. Depending on the sign of the exchange integral J_{ex} the spins can align parallel or anti-parallel [5]. The exchange energy E_{ex} will be at minimum when the spins are parallel to each other when $J_{ex} > 0$. If $J_{ex} < 0$ the minimum energy E_{ex} can be observed when the spins align anti-parallel as shown in figure 1.14.

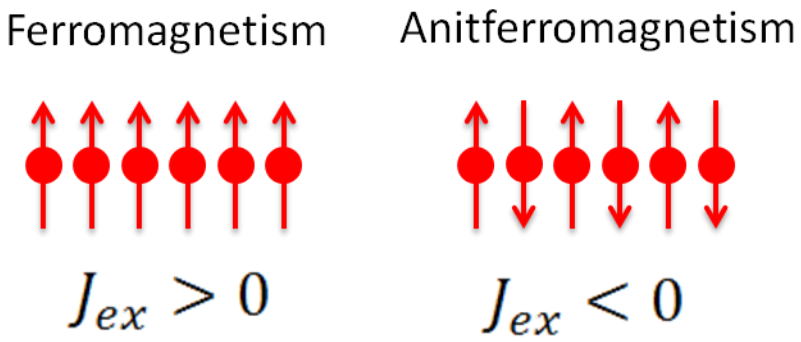

Figure 1.4: A crude representation of the spin orientation in ferro and anti-ferro magnetism when E_{ex} is at a minimum.

This is the mechanism that is responsible for ferromagnetism ($J_{ex} > 0$) and anti ferromagnetism ($J_{ex} < 0$).

1.3 *Magnetization Processes*

1.3.1 *Introduction*

In the previous sections of this chapter the basic concepts of magnetic free energy were discussed. In this section domain theory and important models that utilize the understanding of the minimum energies of magnetic systems will be considered.

To gain a better understanding of ferromagnetic material we will look briefly at magnetic domains and why they are formed. Following domain theory, the observation of the simplistic case of a single domain particle under the influence of an applied magnetic field with no thermal excitation will be considered. We will then observe the same single domain particle as it is thermally excited and observe the effects it has on the magnetic properties. Finally, we will consider an assembly of interacting particle and focus on the observation of how they interact in an applied field and amongst themselves.

1.3.2 *Domain Theory*

Equipped with a basic understanding of magnetism and ferromagnetic materials and a grasp of the energies associated with magnetic material mentioned in section 1.1, we can now briefly discuss magnetic domains. With the image of the orientation of the spins in a ferromagnetic material in mind (figure 1.4), we could assume that the bulk of the spins in the material would always face the same way, but this is not the case. The spins in ferromagnetic material tend to form groups or domains that are oriented in different directions to minimize the energy of the system. In each domain, the spins in the material are oriented in the same direction. Bloch walls, a type of domain wall for bulk materials (see figure 1.5(a)), in a crystal separate adjacent domains magnetized in different directions [5]. Another type of domain wall that can be produced is Neél walls. Neél walls occur when the thickness of the ferromagnetic material becomes comparable to the size of the Bloch wall. The rotation of the moments in Néel walls are no longer 3-D (Bloch walls), but 2-D in the plane of the film (see figure 1.5(b)). Bloch and Néel walls cost exchange energy to create and as a consequence there are a finite number of walls that can be created. The change in orientation of the spins is done gradually over many spins, crudely shown in figure 1.5.

Two main magnetization processes occur in bulk magnetic material, domain wall motion and domain (magnetization) rotation. As magnetic field is applied to bulk magnetic material the domain walls tend to move and shift until a single domain is created, and finally rotating to align with the field.

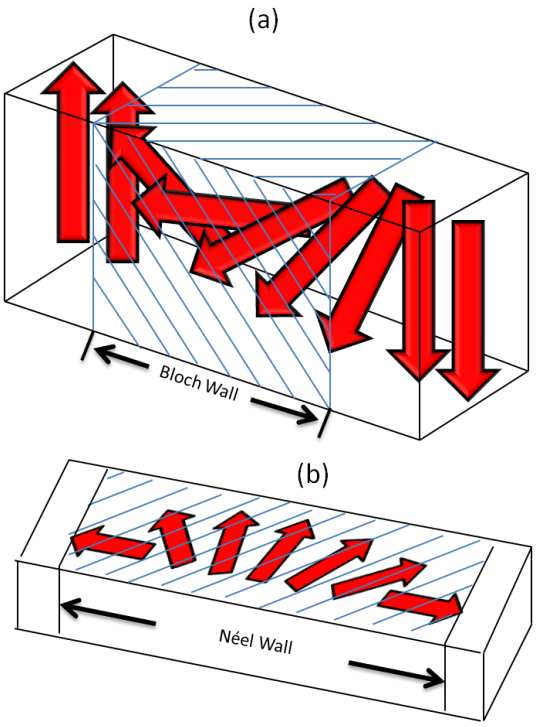

Figure 1.5: Rotation of moments (represented by the red arrows) to form Bloch walls (a) and Néel walls.

Multi-domain systems have proven to be difficult to predict and to model because of the complex nature of domain wall movement as well as many other interactions. As the size of a particle is decreased and becomes comparable to the size the Bloch walls a single domain or monodomain can be obtained due to competing energies of the domain walls and the magnetic anisotropy. The size of such a particle is typically 10-100nm in diameter [5]. For example, the magnetic systems studied throughout this thesis fall close to the same dimensional category as single domain particles. As a consequence, we can approximate such systems after a single domain model which will be explained in the next section.

1.3.3 *Stoner-Wohlfarth Model*

The behavior of a single domain particle was first modeled by Stoner and Wohlfarth in 1948 [6]. The Stoner-Wohlfath (SW) model or coherent rotation model [3] is the simplest model which can predict ferromagnetic switching behavior, one of the most important features for magnetic data storage [7]. The SW model is based on the following assumptions: 1) thermal relaxation effects are neglected (the temperature is 0 Kelvin), 2) the particle is a single domain elongated spheroid with uniaxial anisotropy 3) all spins rotate coherently therefore the net spins can be summed as one giant moment 4) the particles are not interacting with each other.

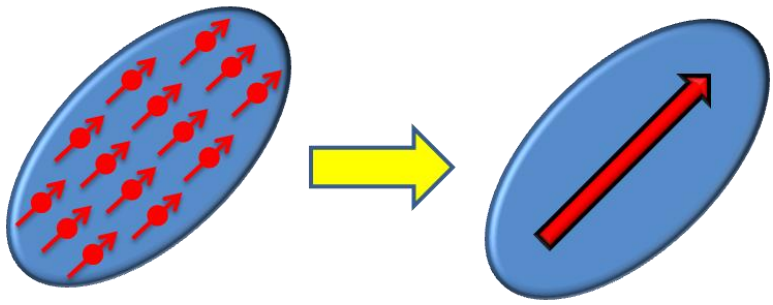

Figure 1.6: Example of a single domain particle

In the following one considers the total energy of a single monodomain (figure 1.6) non-interacting particle with uniaxial anisotropy under the influence of an applied magnetic field as in figure1.7. The magnetization is now subjected to the competing effects of the uniaxial anisotropy energy and the energy of the external applied field [7].

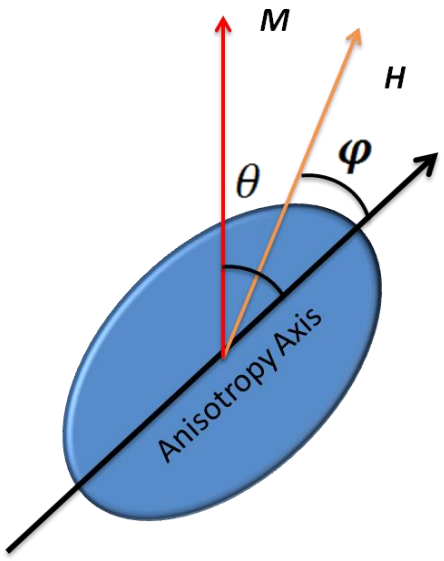

Figure 1.7: Particle with uniaxel anisotropy in an applied field H.

The total energy density of the monodomain particle can be written in terms of the anistropy energy E_A and the Zeeman energy E_Z

$$E_T = E_A + E_Z. \tag{1.18}$$

The energy can also be written as

$$E_T = Ksin^2\theta - \boldsymbol{M} * \boldsymbol{H}, \tag{1.19}$$

where K is the anisotropy constant, $\boldsymbol{M}$ is the magnetization and $\boldsymbol{H}$ is the applied magnetic field. Appling the dot product we find

$$E_T = Ksin^2\theta - HM_s \cos(\theta - \varphi) \tag{1.20}$$

where θ is the angle between the magnetization $\boldsymbol{M}$ and the easy axis , φ is the angle between the applied field $\boldsymbol{H}$ and the easy axis, and M_s is the saturation magnetization. Let $\theta = \theta^*$ at equilibrium, and minimize the energy to find the equilibrium position of M_s and the critical

angle at which the magnetization switches. Take the first and second derivatives with respect to θ:

$$\left(\frac{dE_T}{d\theta}\right)_{\theta=\theta^*} = 0 \quad \text{and} \quad \left(\frac{d^2E_T}{d\theta^2}\right)_{\theta=\theta^*} \geq 0. \tag{1.21}$$

We find that

$$\left(\frac{dE_T}{d\theta}\right)_{\theta=\theta^*} = [2Ksin\theta cos\theta - HM_s \sin(\theta-\varphi)]_{\theta=\theta^*} = 0, \tag{1.22}$$

where the magnetization component is just

$$M = M_s \cos(\theta-\varphi). \tag{1.23}$$

At φ=90^o the magnetization M is a linear function of H showing no hysteresis

$$2K\frac{M}{M_s} = HM_s\,, \tag{1.24}$$

with $M/M_s = m$, the normalized magnetization

$$m = \frac{HM_s}{2K}. \tag{1.25}$$

Saturation magnetization is achieved when $H = H_k = (2K/M_s)$, which is the anisotropy field. $H/H_k = h$ is the normalized field. Writing the derivatives in terms of the normalized field

$$\left(\frac{dE_T}{d\theta}\right)_{\theta=\theta^*} = [sin\theta cos\theta - h\sin(\theta-\varphi)]_{\theta=\theta^*} = 0 \tag{1.26}$$

$$\left(\frac{d^2E_T}{d\theta^2}\right)_{\theta=\theta^*} = \cos(2\theta) + hcos(\theta-\varphi) > 0 \tag{1.27}$$

The critical field and angle can be written as

$$tan^3\theta_c = -tan\varphi \tag{1.28}$$

and

$$h_c{}^2 = 1 - \frac{3}{4}sin^2 2\theta_c \,. \tag{1.29}$$

When $\theta_c = 0$ and $\varphi = 0$ a rectangular hysteresis loop is produced, as shown in figure (1.8).

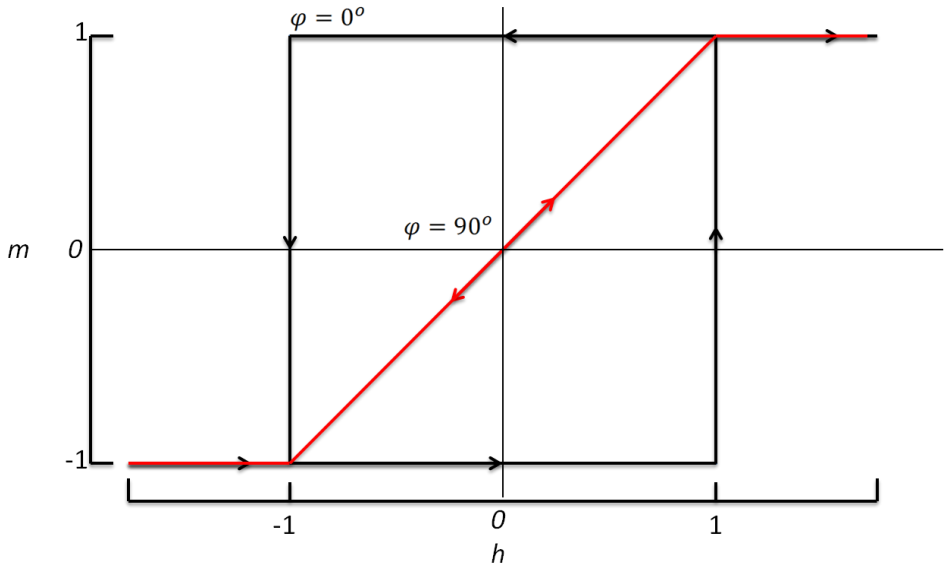

Figure 1.8: 0 and 90 degree magnetization loops of a single domain particle.

The resulting equations give rise to the Stoner-Wohlfarth astroid curve (figure 1.9) which is the locus of critical switching fields.

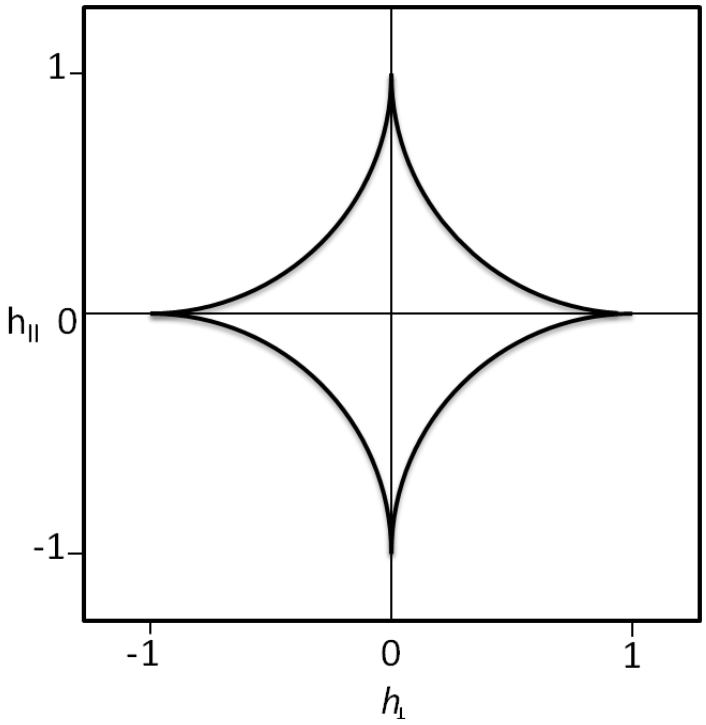

Figure 1.9: Stoner-Wolfarth asteroid. Switching can only occur inside the asteroid.

1.3.4 *Néel-Brown Model*

A brief discussion of thermal effect on particles will be explored in this section. In idealized systems when particles are not interacting and with no thermal excitation, the Stoner-Wohlfarth model can be applied. However, the SW model fails when particles are thermally excited.

As an ideal single domain particle or nanoparticle undergoes thermal excitation the moments tend to decay exponentially toward thermal equilibrium [8]. The theory of thermal relaxation was first proposed by Néel [9] and later developed by Brown [10]. Bean [11] later coined the behavior of such magnetic systems as superparamagnetic. Both Néel and Brown assumed an ideal particle and derived a single time for relaxation [8]. The pre-exponential factor

is the main difference between the authors' approaches in the development of the theory. The pre-factor consists of several factors such as damping and temperature; for simplicity, assumed to be constant. The Néel-Brown model gives the time τ for an ideal particle to spontaneously switch its magnetization by overcoming the anisotropy energy barrier $\Delta E = KV$, where K the anisotropy is constant, V is the volume of the particle at a given temperature T.

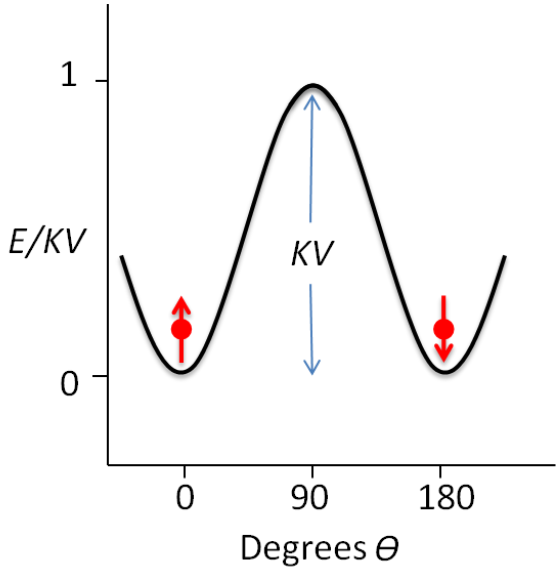

Figure 1.10: Energy barrier with a height of KV.

The time constant for magnetic reversal can be written as

$$\tau = \tau_o e^{\frac{KV}{kT}}, \tag{1.30}$$

where k is the Boltzmann constant, T is the temperature, and $\tau_o = 10^{-9}s$. The magnetic behavior of the system is strongly dependent on the measurement time frame or window τ_m in which the measurement is desired. If $\tau_m \gg \tau$ then the thermal relaxation is very fast and the energy barrier is overcome easily and the system exhibits superparamagnetic behavior(red curve

in figure (1.11)). If $\tau_m \ll \tau$ then the relaxation time is slower and the system is stable exhibiting ferromagnetic behavior (blue curve in figure 1.11).

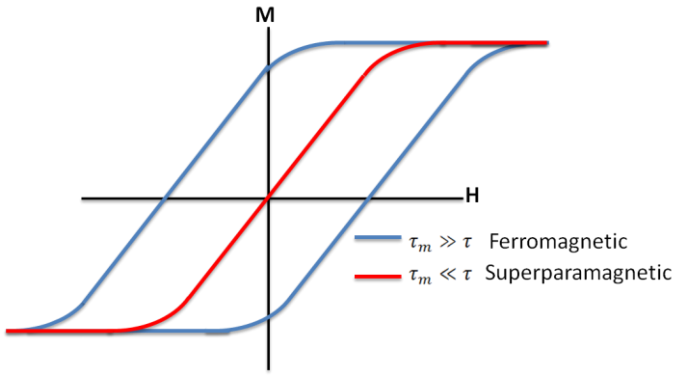

Figure 1.11: Example of (Blue) ferromagnetic behavior, and (Red) superparamagnetic behavior.

The temperature that separates the superparamagnetic regime and blocking one is called the blocking temperature T_B [12]. The blocking temperature is defined as the temperature at which the relaxation is becomes equal with the measurement time $\tau_m = \tau$. For conventional magnetometry methods the measurement time is assumed to be of the order of 10^2 seconds and in this case and T_B is

$$T_B = \frac{KV}{25k}. \tag{1.30}$$

In this thesis we studied the static magnetic properties of several magnetic systems using magnetometry methods, ad for which the thermal relaxation effects could be neglected.

1.3.5 *The Classical Preisach Model*

The two models in the previous sections assumed that a single particle or maybe an assembly of particles were non-interacting. We also discussed a system was exposed to thermal excitation (Néel-Brown). In this section the interaction between particles will be considered.

In 1935 Preisach extended the understanding of hysteretic behavior exhibited by ferromagnetic materials [13].The classical Preisach model makes the following assumptions: The major hysteresis loop of a given ferromagnetic specimen consists of an infinite number of square hysteresis loops known as hysterons, and does not take into account stress, temperature dependence, frequency dependence, and so on.

While the Preisach model has been adapted to many other hysteretic systems, in this thesis we will focus on the application of the model to ferromagnetic systems and view the hysterons in magnetic terms as in figure 1.12.

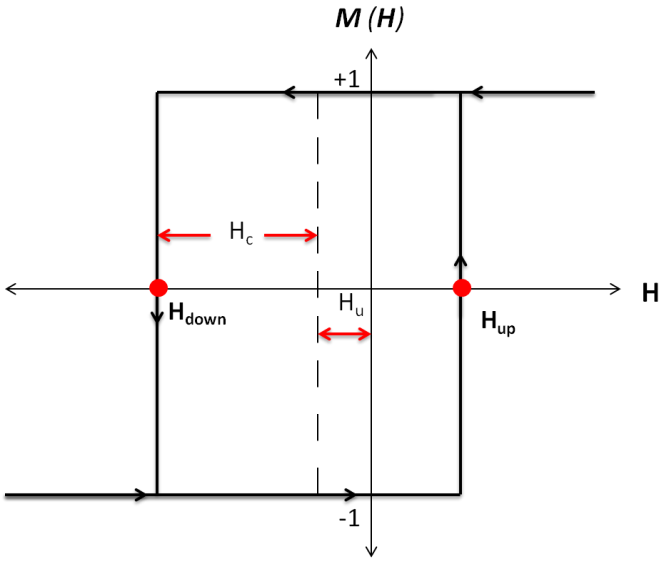

Figure 1.12 shows a graphical representation of a hysteron.

The behavior of magnetic system in the Preisach model can be described by a distribution the hysterons ($\hat{\gamma}_{H_{up},H_{down}}$). Each hysteron has associated threshold reversal fields *up* (H_{up}) and *down* (H_{down}) as saturation magnetization $+M_{sat}(+1)$ switches from $-M_{sat}(-1)$ back to $+M_{sat}(+1)$. In an assembly of interacting particles the associated hysteron of the particle

experiences an offset or biasing from the origin (figure 1.12). The shift of the hysteron is a measure of the interaction field acting on that specific particle from its sounding neighbors.

In order to be considered a classical Preisach system the following conditions must be satisfied: 1) the deletion and 2) the congruency properties. The deletion property is met by each minor loop starting and ending at the same point on the major hysteresis loop (figure 1.13(a)) [14]. Therefore, the history is "deleted." The congruency property is met by all minor loops, with the same upper and lower field limits, must be congruent geometrically [14] as shown in figure 1.13(b).

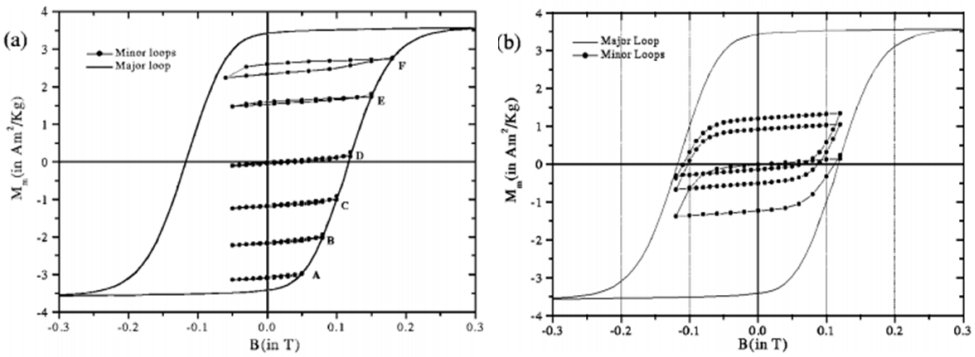

Figure 1.13: (a) the deletion property and (b) the congruency property.[14]

A function $\rho(H_{up}, H_{down})$ determines the weight of each hysteron and is known as the weight or density function. A set of these weight functions is the Preisach distribution and we will see later how to determine such a function.

The Preisach model can be written as

$$M = \iint_{H_{up} \geq H_{down}} \rho(H_{up}, H_{down}) \hat{\gamma}_{H_{up}, H_{down}} \, dH_{up} dH_{down} \quad , \tag{1.31}$$

where M is the magnetization determined by the hysterons $\hat{\gamma}_{H_{up},H_{down}}$ and the weight function $\rho(H_{up}, H_{down})$. The Preisach plane is

$$P = \{(H_{up}, H_{down} | H_{up} \geq H_{down}\} \tag{1.32}$$

where (H_{up}, H_{down}) is a point in the Preisach plane. The Preisach plane is shown in figure 1.14.

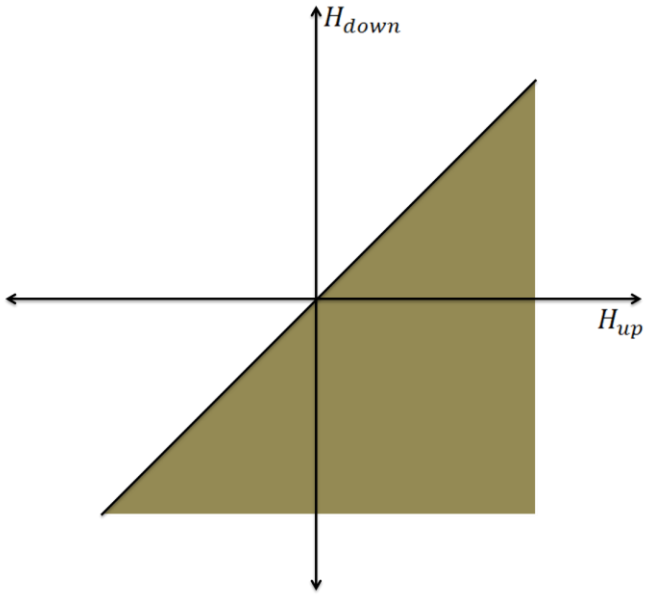

Figure 1.14: Preisach plane

At each point (H_{up}, H_{down}) there is an associated hysteron. We can now view the Preisach plane with each point in the plane represented by a hysteron as shown in figure 1.14.

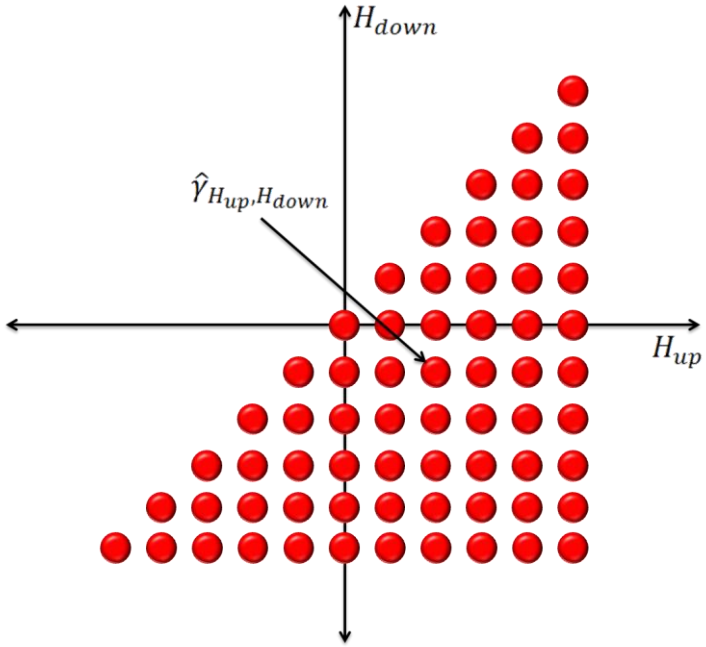

Figure 1.15: Preisach plane with each point representing a hysteron.

We can now determine the set of weight functions $\rho(H_{up}, H_{down})$.

Consider the major hysteresis loop of an arbitrary specimen. Beginning at a saturating field where all the hysterons are in the *up* position (figure 1.16a), and as the applied field is decreased, the switching of the hysterons begin from *up* to *down* or from +1 to -1 (figure 1.16b).

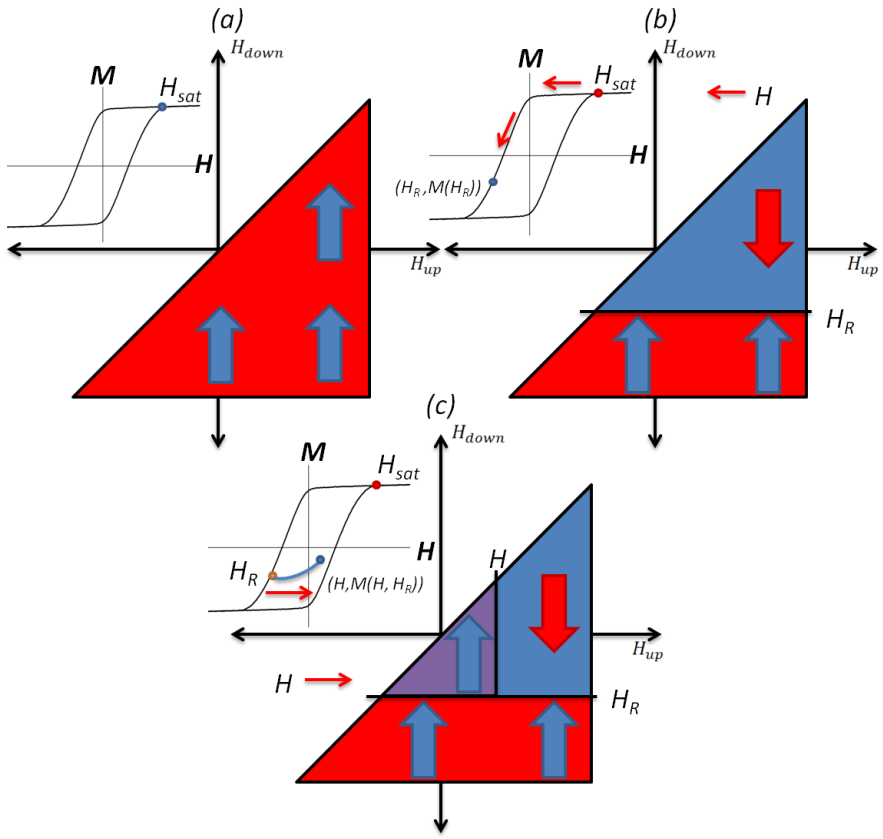

Figure 1.16: Graphical representation of the Preisach model. (a) H=H_{sat} where all hysterons are in the up position, (b) a field is applied to a reversal point H_R, and (c) the looped is probed as the field is applied.

The magnetization in (figure 1.16b) can be written as a function of the reversal field

$$M(H_R) = \iint_{P^+} \rho(H_{up}, H_{down}) \hat{\gamma}_{H_{up},H_{down}} \, dH_{up} dH_{down} + \iint_{P^-} \rho(H_{up}, H_{down}) \hat{\gamma}_{H_{up},H_{down}} \, dH_{up} dH_{down} \quad , \quad (1.32)$$

where P^+ and P^- represent the up and down hysterons, respectively. The hysterons operator is assigned a +1 or -1 depending on the state of the hysterons and the magnetization can now be simplified to be

$$M(H_R) = \iint_{P^+} \rho(H_{up}, H_{down}) \, dH_{up} dH_{down} - \iint_{P^-} \rho(H_{up}, H_{down}) \, dH_{up} dH_{down} \quad , \quad (1.33)$$

Next we can write the magnetization of (figure 1.16c) as a function of the applied field and the reversal field

$$M(H,H_R)=\iint_{P^+}\rho(H_{up},H_{down})\,dH_{up}dH_{down}-\iint_{P^-}\rho(H_{up},H_{down})\,dH_{up}dH_{down}+\iint_{\acute{P}(H,H_R)}\rho(H_{up},H_{down})\,dH_{up}dH_{down}\quad,\tag{1.34}$$

where third integral is the area of the small triangle in (figure 1..16c). Then the difference of the magnetizations $[M(H_R)-M(H,H_R)]$ is

$$M(H_R)-M(H,H_R)=-2\iint_{\acute{P}(H,H_R)}\rho(H_{up},H_{down})dH_{up}dH_{down}\quad.\tag{1.35}$$

From the figure the orientation of the hysterons are *down,* so now solving for the weight function we find

$$\rho(H,H_R)=\frac{1}{2}\frac{\partial^2}{\partial H\partial H_R}[M(H_R)-M(H,H_R)].\tag{1.36}$$

The first term will be zero since $M(H_R)$ is only a function of H_R then

$$\rho(H_R,H)=-\frac{1}{2}\frac{\partial^2 M(H,H_R)}{\partial H\partial H_R},\tag{1.37}$$

the weight function in terms of the applied field H and the reversal field H_R. The set of weight functions is known as the Preisach distribution.

To experimental obtain the Preisach distribution Mayergoys[15] introduced First order reversal curve (FORC) as an identification method. Systems such as magnetic nanowires arrarys

closely meet the requirements to be consider a classical Preisach system as shown by Sorop et al [14]. As we will see in the next chapter the FORC method can be used to obtain the Priesach distribution.

Chapter 2: *Experimental Techniques*

2.1 *Introduction*

Ferromagnetic magnetic materials have revolutionized the technological industry because of their unique hysteretic characteristics. To be considered hysteretic a system must have several possible outputs for every given input. As an applied magnetic field ***H*** (input) is cycled there are in general two paths that the magnetization **M** (output) follows when a specimen is saturated. The switching property is one the main desired characteristics of ferromagnets because of their application in computers and other information storage devices. Many methods are used to characterize ferromagnetic material. For example, the major hysteresis loop and first order reversal curve method, as described below, are quickly becoming the standard protocol for studying and characterizing ferromagnetic magnetic materials. This chapter will be devoted to describing the experimental methods utilized to synthesize and characterize the magnetic materials used throughout the rest of this thesis.

2.1.1 *Major Hysteresis Loop*

The major hysteresis loop (MHL) is one of the main characteristics of ferromagnetic material. Known for the simplicity with which it can be obtained, the MHL can be considered the *fingerprint* of ferromagnetic material [16]. Obtaining the MHL is one of the first steps in the protocol for characterizing a ferromagnetic material. With recent advances in electronics, more efficient manufacturing in machinery, and improvements in data processing methods, magnetization curves can be obtained easily within minutes.

Consider a ferromagnetic sample under the influence of a positive applied field. The specimen will reach a state of saturation magnetization as a large enough field is applied. Once the specimen has reached saturation magnetization the applied field ***H*** is reversed until the sample reaches negative saturation. In general, a sample is saturated with ***H*** in the positive direction and then data are recorded while the field is cycled from positive to negative and back to positive.

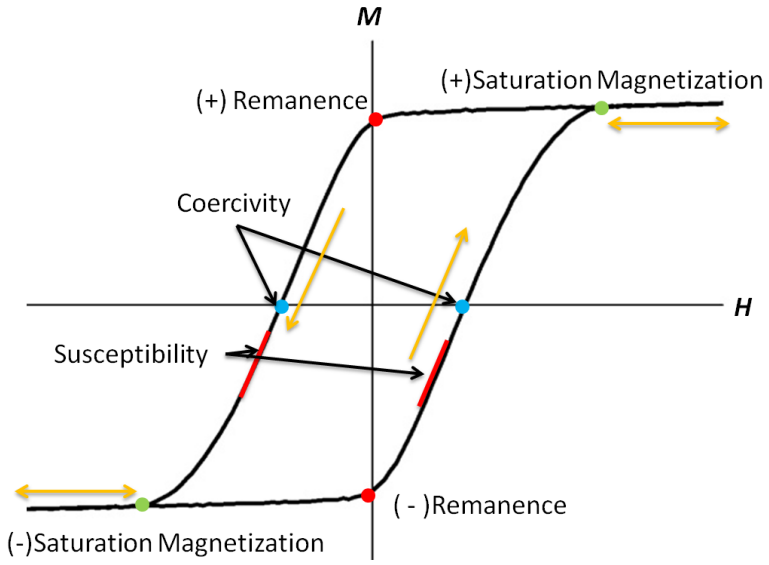

Figure 2.1: The major hysteresis loop and associated main parameters

The above figure is an example of an experimentally obtained MHL using a vibrating sample magnetometer. With a large enough positive applied field ***H*** a given specimen can be saturated magnetically. Saturation magnetization occurs when all domains are aligned with the applied field ***H***. As ***H*** is reduced to zero we find that the magnetization curve does not return to zero when ***H*** is zero. In fact, the specimen will retain a certain magnetization with no applied field. This is known as the positive remanence, and it is the point where a permanent magnetization can be obtained. In order to return the magnetization back to zero a negative applied field ***H*** is

needed. The value of the applied field ***H*** when the magnetization returns to zero is known as the coercivity. This is a measure of amount of field needed to "push" the magnetization to zero, obtaining a demagnetized state that is actually not the same as the original state of demagnetization. If a negative field ***H*** is applied, the specimen reaches a negative saturation magnetization. Finally, applying a positive field ***H*** the lower path of the MHL is taken, passing through its associated negative remanence and coercivity. The path direction is marked with arrows in figure 2.1.

Although the MHL provides some useful information about a given specimen it fails to produce an adequate description of the magnetic interactions. Different protocols such as the ratio of remnant magnetization to saturation magnetization (squareness) and sheerness of the MHL proved to be unsuitable tools in the further characterization of ferromagnetic material [17, 18]. More complex magnetization curves that actually probe the interior of the MHL, such as *higher-order* magnetization, curves can provide additional information that can be used to further characterize ferromagnetic material by revealing magnetic interactions [19, 20]. Higher-order magnetization curves are obtained after a number of reversals of the applied ***H*.** Thus, the MHL can be considered a zero-order magnetization curve and all subsequent curves when the applied field is reversed at a certain point on the MHL can be considered higher-order. To be more specific, positively saturating a specimen then allowing the magnetic field to decrease to a point on the descending branch of the MHL and reversing the polarity of the field before the negative saturation is considered a first-order reversal. This process can be extended to second and third-order and so on depending on how many field reversals are desired. For the purpose of this thesis we will only be considering first-order reversals, as we will see in the next section.

2.1.2 *First Order Reversal Curve Method*

In order to probe the interaction effect of magnetic assembles of particles several methods of higher-order magnetization protocols were proposed. Examples of higher-order curves are Henkel plots [21], δM plots[22], and first-order reversal curves [20, 21, 23]. As mentioned in Chapter 1, Mayergoys [20] first introduced first order reversal curve (FORC) measurement as an identification method for the Preisach model. It was later implemented by Pike who showed that the FORC method of characterization was a better alternative than δM plots for the study of magnetic interactions in assembles of magnetic entities [23]. The FORC method is experimentally easier to achieve. It also requires the system to be magnetically saturated which is highly reproducible. Also, as mentioned in chapter 1, the FORC method is independent of the Preisach model in the sense that it can be applied to any system that exhibits hysteretic behavior.

The FORC method of characterization became an important characterization tool in many interacting hysteretic systems for a multitude of different materials ranging from magnetic [24-31] and electric [32, 33] to spin transition [34-37]. FORC has proven to be a useful tool to study the change in interactions throughout a series of samples that have few variables. In the next section we will look at the experimental methods used to obtain FORCs.

2.1.2.1 *Experimental first order reversal curve measurements*

An experimental set of FORCs, commonly called a family of FORCs, consists of many minor hysteresis curves. Typically a family of FORCs of approximately 100 minor loops is needed to gain adequate detail of the magnetic properties. The simplicity in which the FORCs can be obtained makes this method a powerful and important tool in magnetic characterization.

Using conventional magnetometry (i.e., vibrating sample magnetometer, alternating gradient magnetometer) a family of FORCs can be obtained in approximately two hours. The measurement time may vary of course depending on the system under study.

A FORC measurement starts by saturating a specimen magnetically by applying a high enough magnetic field ***H***, in the direction chosen to be positive. Following saturation, the field's polarity is changed and ramped down following the top branch of the MHL to a reversal point chosen to premature to negative saturation magnetization.

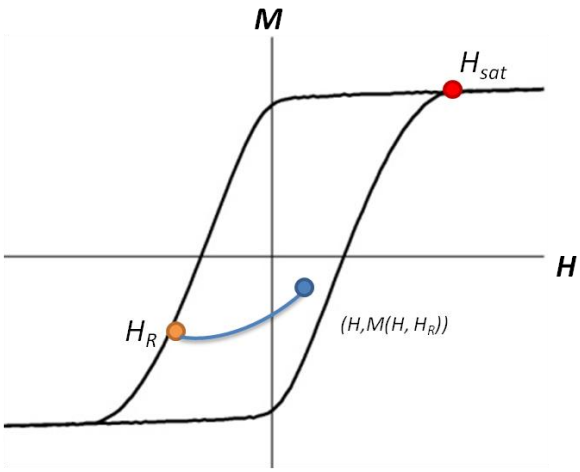

Figure 2.2: An example of a single first order reversal curve probing the inside of the major hysteresis loop at an arbitray reversal field H_R.

The reversal point will be defined as H_R as shown in figure 2.2. The field is then reversed back to the positive direction and magnetization is recorded as function of the applied ***H*** field and reversal field H_R as the field is ramped back to positive saturation magnetization. This process is repeated until the interior of the MHL mapped out by FORCs as shown in figure 2.3 below.

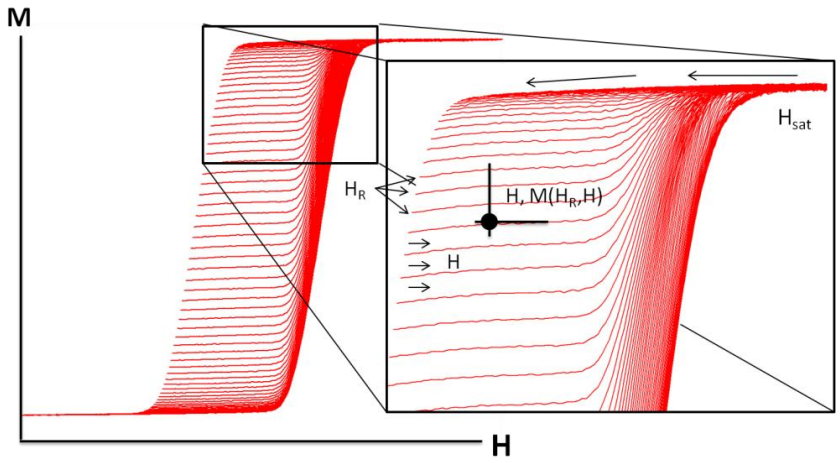

Figure 2.3: Experimentally obtained family of FORCs where the interior of the MHL is completely probed.

Different methods to obtain a family of FORCs were explored during the research for this thesis in an attempt to optimize the results of the measurements. All of the methods have certain drawbacks and advantages. Each process starts with complete magnetic saturation of a given specimen as described above.

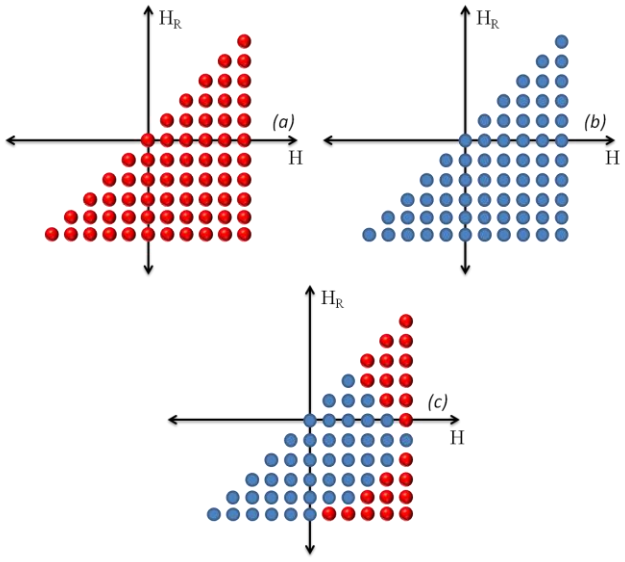

Figure 2.4 (a) The FORC plane, where each red dot represents a hysteron. (b)The experimental plot for obtaining the extended FORC. (c)The default arrangement for the Princeton Measurement VSM/AGM.

Figure 2.4(a) above is an example of the Preisach plane or now the FORC plane where each red dot represents a hysteron. The *extended FORC* is shown in figure 2.4(b) obtained by taking FORCs from positive saturation to negative saturation. The advantage of *extended FORC* is that it collects everything, which is also one of its drawbacks. *Extended FORC* measurements acquire a lot of data that is not needed and this in turn causes the resolution of the FORC distribution to be compromised to a certain degree. Figure 2.4(c) is the default program for the Princeton measurement VSM for obtaining FORCs. This program allows the user to choose where the first FORC will begin. The main advantage of this method is it clips out the unwanted data as seen in red in figure 2.4(c). After each FORC is taken the sample is saturated again. The disadvantage is the accidental clipping of the FORC data which will result in hours of time wasted if the user is careless.

2.1.2.2 *FORC distribution calculation*

After a family of FORCs is obtained the second order mixed derivative with respect to the reversal field $\boldsymbol{H}_{\mathrm{R}}$ and the applied field $\boldsymbol{H}$ is applied to amplify and reveal subtle changes in magnetization. The FORC distribution is written as

$$\rho_{FORC}(H_R, H) = -\frac{1}{2}\frac{\partial^2 M(H_R, H)}{\partial H_R \partial H}. \tag{2.1}$$

The above equation takes on a form similar to the Preisach weight function, but as mentioned previously the FORC method can be applied to a variety of hysteretic systems regardless if it fits the Preisach model or not. By applying the second order derivative of the magnetization, the associated noise is also amplified. Typically, a certain amount of noise removal or smoothing is required when calculating a FORC distribution. The FORC distribution can be represented as a 2-D contour plot or as a 3-D plot as in figure 2.5.

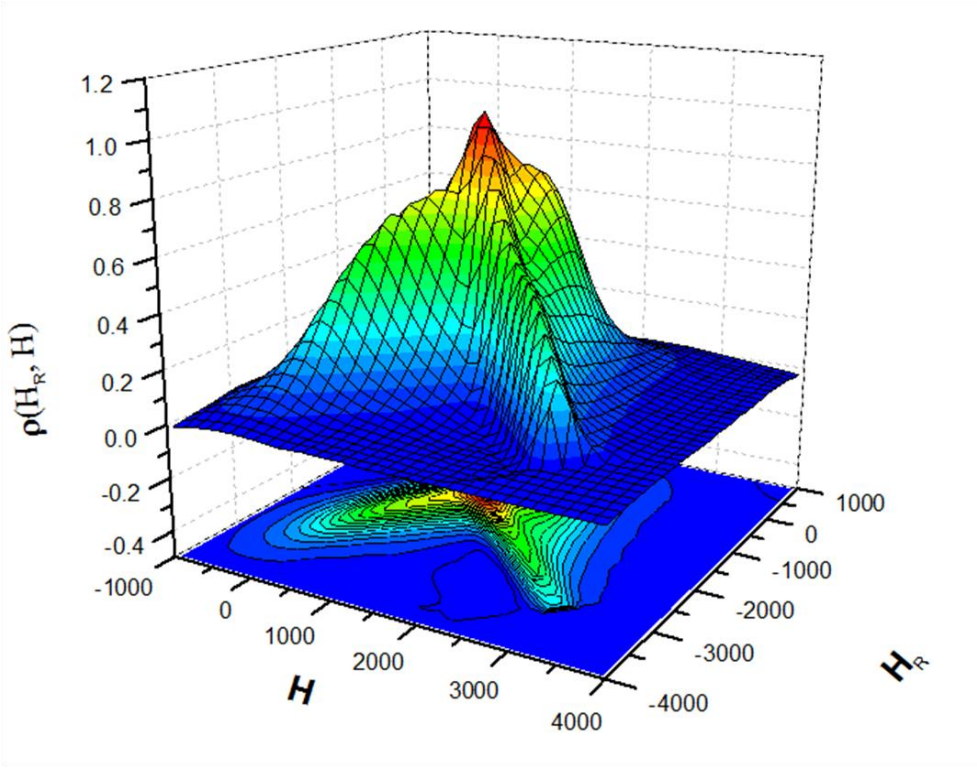

Figure 2.5: ***Graphical representation of a 3-D plot and projected 2-D contour plot as a function of reversal and applied field, H_R and H, respectively.***

2.1.2.2.1 FORCinel

In this section we will briefly describe the computer program used in this research to process the FORC data.

To calculate each FORC distribution a computer program named *FORCinel* [38] that uses locally weighted regression smoothing was implemented. At any point P in the FORC plane, a least square fit to the magnetization M (H_R,H) is performed over a square grid of points surrounding P [38]. The magnetization M (H_R, H) is fitted to a second–order polynomial function. This method most commonly used [23] to calculate FORCs

$$M(H_R, H) = a_1 + a_2 H_R + a_3 H_R^2 + a_4 H + a_5 H^2 + a_6 H_R H. \quad (2.2)$$

Therefore the value of the FORC at point P is equal to $-a_6/2$. The smoothing factor determines the size of the square grid $(2SF+1)^2$ in the (H_R,H) plane. The smoothing factor acts to smooth out the noise, but it can also over smooth and obscure the actually desired data. Typically a small smoothing factor of 2-5 is in the acceptable range. A smoothing factor that is too large will broaden the features of the FORC distribution and skew the results as in figure 2.6c.

When running a FORC experiment it is imperative to ensure that the noise from the measurement it at a minimum. Using material that exhibits a strong ferromagnetic signal, increasing the averaging time between data points, and eliminating most of the material that can give undesirable signals (i.e., substrates, capsules, sample contamination, and so on…) are a few precautionary steps to aid in obtaining excellent FORC measurement results. Figure 2.6 is a comparative result of smoothing factors.

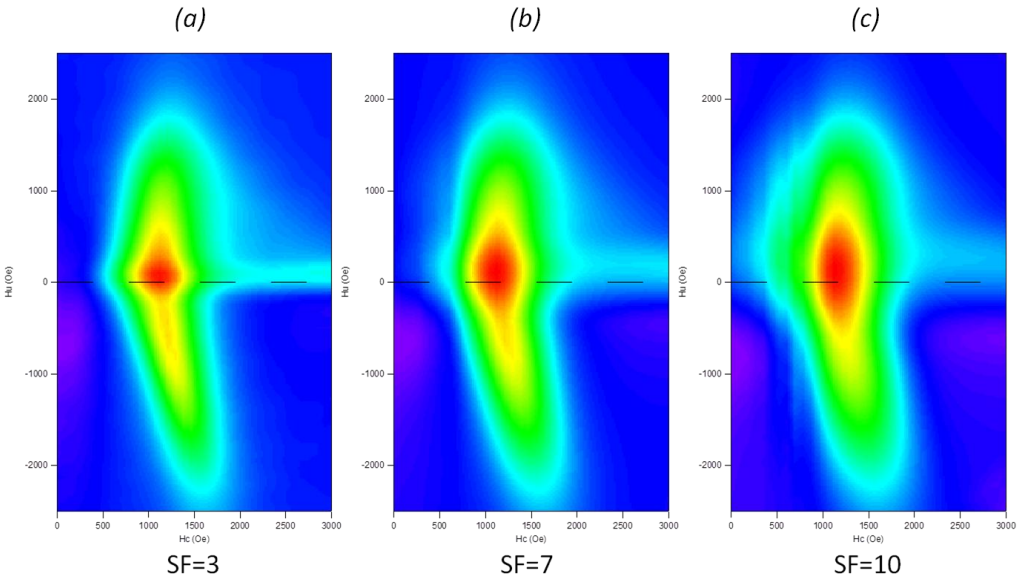

Figure 2.6: ***Experimentally obtained FORC distributions with different smoothing factors. The features in (b) and (c) are broadendue to over smoothing.***

Another feature of FORCinel that aids in the understanding of the FORC results and their relations to the MHL, is the color FORC option. This option provides a qualitative analysis tool by using the same color change to the FORC and the FORC distribution, allowing insight to which portion of the FORC is contributing to the FORC distribution, as shown in figure 2.7.

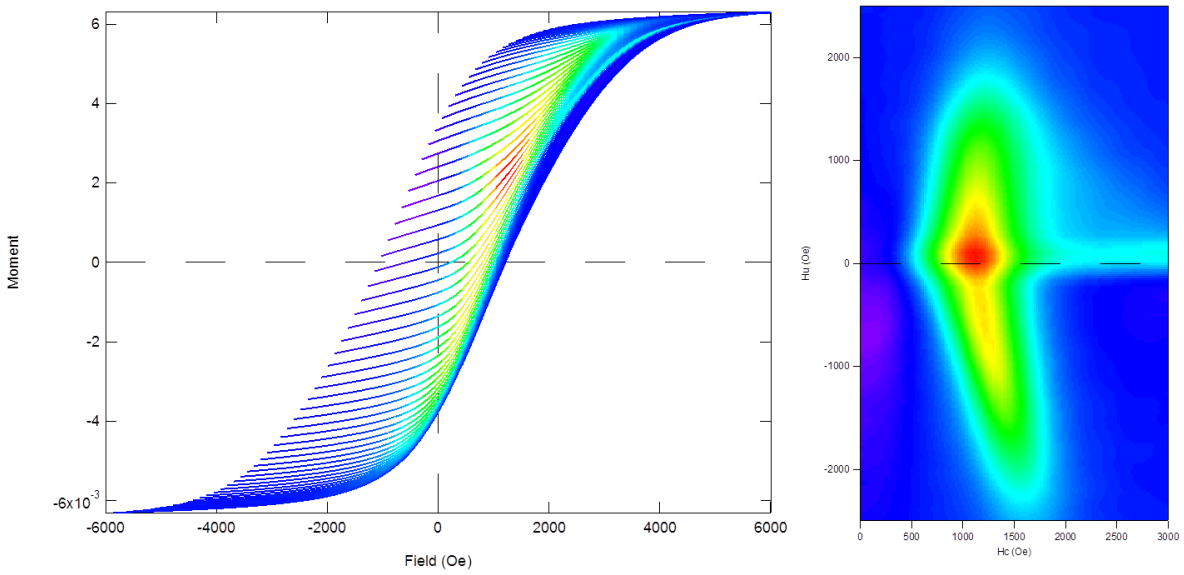

Figure 2.7 ***A colored family of FORCs (left) revealing the potions of the MHL that contribute to the FORC distribution (right).***

2.1.2.3 *Quantitative analysis using FORC*

The FORC method in not only a tool with qualitative analysis capabilities, it allows for a quantitative analysis approach by capturing the distribution of magnetic properties. It is helpful to apply a coordinate change to the FORC distribution for the discussion of the magnetic properties. This is done by considering a hysteron in terms of local coercivity H_c and biasing fields H_u, which affect wideness of the loop and how much the loop is shifted horizontally, respectively. This is shown in Figure 2.8, a graphical representation of a hysteron in terms of local coercivity H_c and biasing fields H_u.

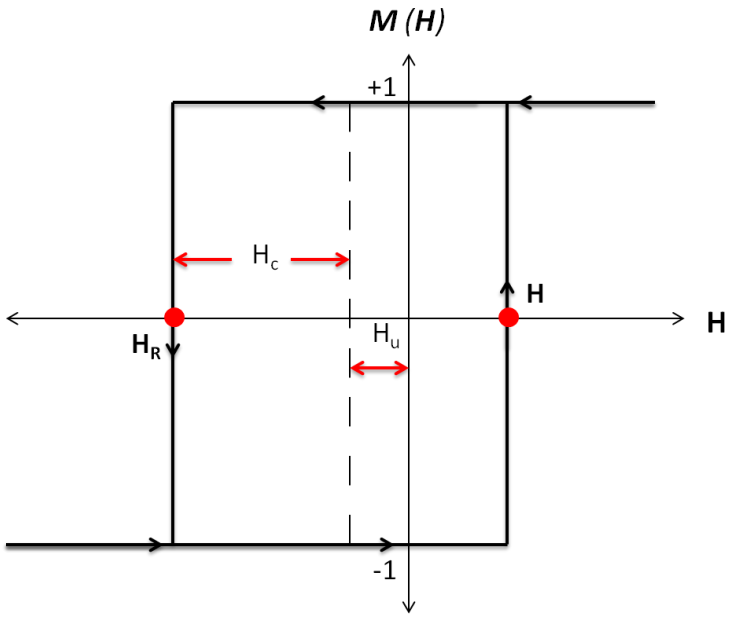

Figure 2.8: A graphical representation of a hysteron in terms of biasing and coercive fields H_u and H_c respectively.

From figure 2.8 it can be seen that the reversal field is

$$H_R = -H_c + H_u, \tag{2.3}$$

and the applied field is

$$H = H_c + H_u. \tag{2.4}$$

By solving for the bias and coercive field we can obtain the new rotated coordinate system

$$H_u = \frac{H+H_R}{2}, \tag{2.5}$$

and

$$H_c = \frac{H-H_R}{2}. \tag{2.6}$$

where, $H \geq H_R$, $H_c \geq 0$ and at the boundary $H \geq H_R$.

The coordinate transformation serves to rotate the distribution 45^o clockwise as shown in figure 2.9.

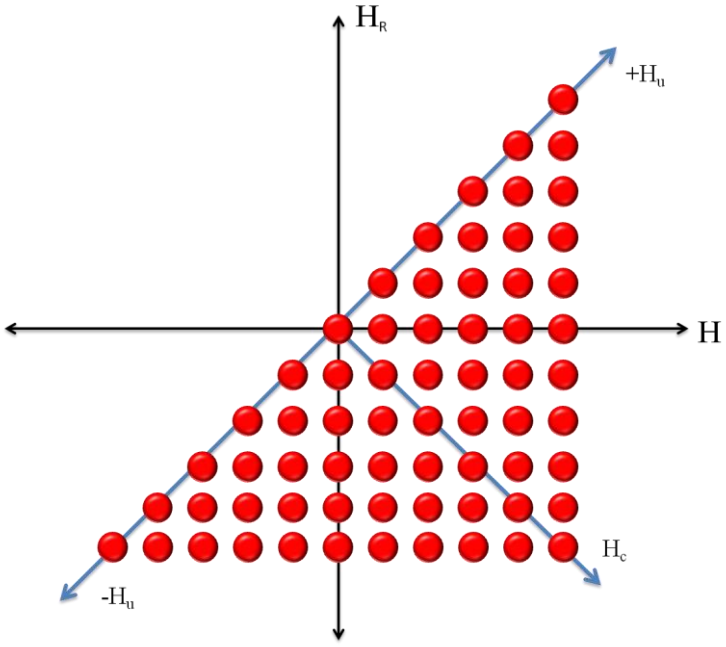

Figure 2.9: FORC plane in the original and rotated coordinated (H,H_R) and (H_c,H_u), respectively.

The blue axes represent the rotated coordinates in terms of biasing and coercive fields. Performing a coordinate change in terms of the biasing interactions and coercivity, complex interacting systems such as ferromagnetic nanowire [16] arrays or ferromagnetic multilayer thin film systems, as we will see later in the thesis, can be studied more readily. As with the original coordinate system the FORC distribution can be plotted as a 2-D contour plot or a 3-D plot.

2.1.2.4 *Switching Field Distribution*

The switching field distribution can give insight to the onset and endpoints of irreversibility [27]. Integrate by integrating the FORC distribution in the original coordinate system $\rho_{FORC}(H_R, H)$ with respect to H

$$\int \rho_{FORC}(H_R, H)\, dH = -\frac{1}{2}\int \frac{\partial M(H_R,H)}{\partial H_R \partial H} dH = -\frac{1}{2}\frac{\partial M(H_R)}{\partial H_R}. \tag{2.7}$$

As shown in figure2.10, by integrating over H we obtain a projection of the switching field distribution onto H_R.

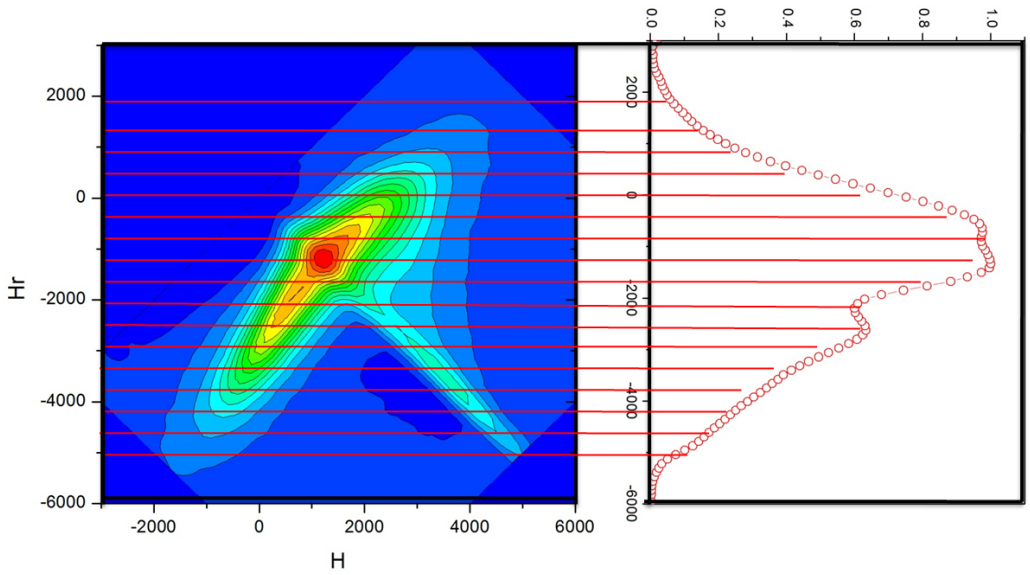

Figure 2.10: The projection of the switching field distribution onto the H_R axis obtained by integrating over H

As shown by Davies et al. [27] the FORC switching field distribution is comparable to that of the DC-demagnetization switching field distribution. The two methods for determining the switching field distribution are fairly different, however. The FORC switching field distribution method is obtained by integrating over the entire FORC which follows the irreversible switching back up to saturation, whereas the DC-demagnetization method probes the remanent state [27].

2.1.2.5 *Projection onto H*

The projection onto the H axis is done by integrating the FORC distribution with respect to H_R

$$\int \rho_{FORC}(H_R, H)\, dH_R = -\frac{1}{2}\int \frac{\partial M(H_R,H)}{\partial H_R \partial H} dH_R = -\frac{1}{2}\frac{\partial M(H)}{\partial H}\,. \tag{2.8}$$

This gives insight to how the magnetization changes as the applied field is changed as the MHL is probed by the FORC.

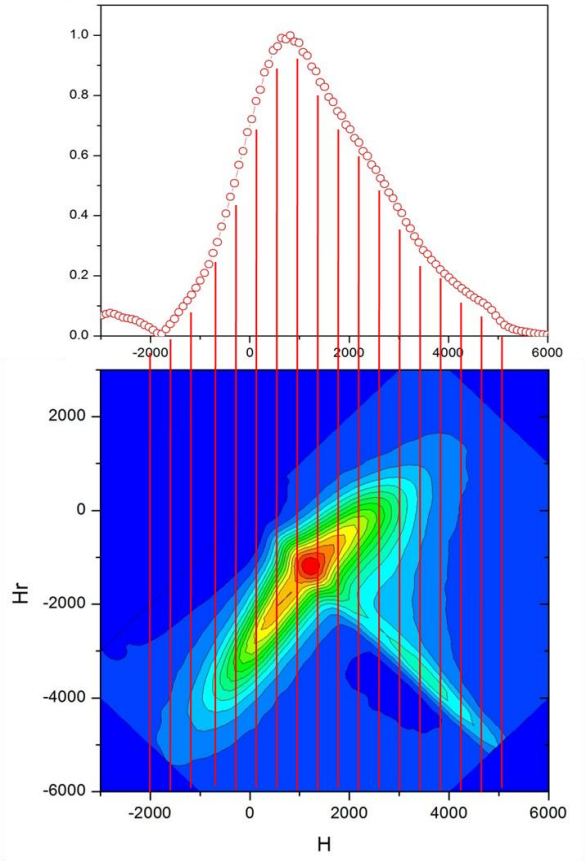

Figure 2.11:The projection of H obtained by integrating over H_R.

2.1.2.6 *Determination of M_{irrev}*

To determine M_{irrev} the total integration of the FORC distribution $\rho_{FORC}(H_R, H)$ is performed

$$\iint \rho_{FORC}(H_R, H)\, dH_R dH = -\frac{1}{2}\iint \frac{\partial M(H_R,H)}{\partial H_R \partial H} dH_R dH = -\frac{1}{2}\frac{\partial^2 M(H_R,H)}{\partial H \partial H_R} = M_{irrev}\,. \tag{2.9}$$

This method is useful when changing system parameters such as introducing impurities or varying layer thickness in thin films by allowing a study of the ferromagnetic phase fraction as the system is altered.

2.1.3 *Sample Synthesis*

2.1.3.1 *Magnetic Nanowires*

Magnetic nanowires have gained much attention in magnetic research in recent years, gaining importance in the class of nanostructured material [39-41]. Due to size confinement, new phenomena arise in these systems which makes them ideal candidates for important technological applications in spintronics and as microwave devices [42-45] high-density recording media, and permanent magnets[46]. For all these applications, as well as in research studies, nanowires are commonly used as highly ordered periodic arrays. Nanowires can be made by depositing suitable composites into nanoporous templates. The nanowires studied throughout the research in this thesis were grown by electrodeposition techniques, which have advantages over the standard preparation methods of nanowires by lithographic approaches. There are several nanoporous materials that can be used as templates but the most common for unidimensional nanostructures are anodic porous alumina and track-etched polymer membranes [47, 48]. These membranes allow fabrication of uniform arrays of metallic nanowires with large-aspect ratios over a large range of wire diameters and interwire distances. The strength of magnetic interactions in magnetic nanowire arrays can be controlled effectively by varying the interwire spacing. The spacing provided by the polymer membranes is difficult to control due to the randomness of pore location obtained through the combination of the charged-particle bombardment (irradiation) and chemical etching [48, 49]. Despite recent progress in

fabrication of ion track nanochannels that allows a better control of the number of the pores in a membrane, their precise location is still problematic [50].

Templates obtained by aluminum anodization provide for better control of the pores through a combination voltage, acid concentration, and time used during the oxidation [48] process. Moreover, through a multistep anodization scheme one can obtain alumina membranes with more complex configurations that can be used to prepare nanowires with modulated diameters and/or varying interwire distances [51].This section will be an overview on the synthesis of nanoporous templates and the growth of nanowires used in this thesis research.

2.1.3.1.1 Aluminum Anodized Oxide (AAO) Template Fabrication

Here we focus on Ni wires deposited in anodic aluminum oxide (AAO) membranes. The membranes were prepared by either a two- or three-step anodization procedure[52]. To prepare the standard mild AAO (Mi AAO) membranes by the two-step method, first an Al film with a thickness of 0.25 mm was annealed at 450 ◦ C for 5 h in Ar atmosphere, and then the sample was electropolished in a 1:4 (volume ratio) solution of perchloric acid-ethanol at 25 V, 10 ◦ C, before anodization in 0.3 M oxalic acid at 40 V, 17 ◦ C. After the oxide layer was removed at 80 ◦ C in a solution of 1.8 wt% chromic acid-5 wt% phosphoric acid, a second anodization was performed in oxalic acid resulting in Mi AAO.

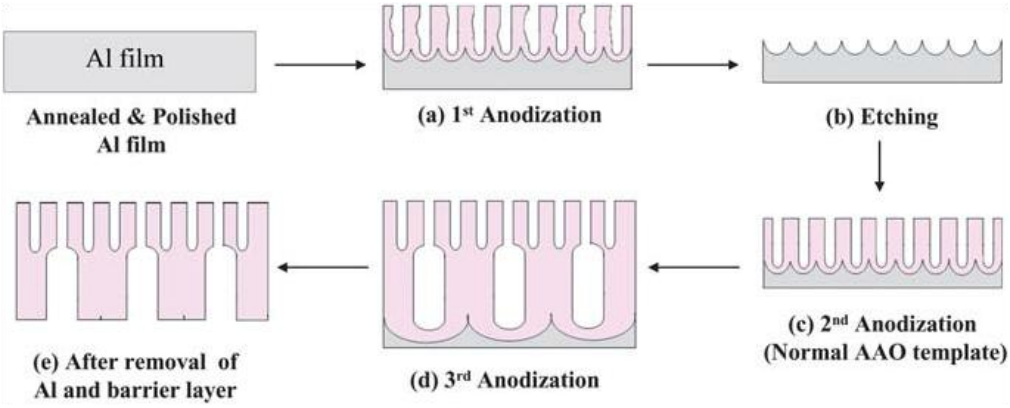

Figure 2.12: ***The two and three step anodization process used in the fabrication of the Mild and Mild Hard AAO templates***

2.1.3.1.2 Nanowire Deposition

The nanowires in the research described in this thesis were deposited in the pores of an AAO template by electrodeposition. An initial thin coat of Ag was deposited onto the template to form an electrode. A counter electrode of Pt was used. An aqueous solution containing metal sulfate was used as the electrolyte. A commercial high-purity of Nickel sulphamate ($NiSO_4$ $7H_2O$ from TECHNIC NC) was use to synthesize the magnetic nanowire arrys. The process was developed using DC electrodeposition method in galvanostatic (constant current) mode, using a Teflon bath cell.

The magnetic Ni nanowires used is this research were deposited as follows: To produce the mild nanowires (Mi) the wires were deposited into the AAO-Mi temple. As for the Mild-Hard nanowires (MiHa) and Hard-Mild nanowires (HaMi), referring to figure 2.12(e) the wires were either deposited into the smaller or larger diameter side of the template, respectively. By filling the pores from the hard side and crossing the MiHa-HaMi interface a single modulated nanowire structure was obtained.

2.1.4 *Vibrating Sample Magnetometer*

The vibrating sample magnetometer (VSM) is diverse as well as sensitive. In 1956 G.W.Van Oosterhout and P.J. Flanders both published the idea behind the VSM, but it was S. Foner who gained credit for creating this instrument. While able to measure strongly magnetic material, the VSM also has the capability to measure precisely small magnetic moments in materials, on the order of ~10^{-5} emu. Using a conventional electromagnet set up a maximum of ~2.2 tesla can be reached. Most VSM companies offer additional attachment options such as high a temperature furnace and cryostat with a temperature range of 4.2K -1000K, none of which were used during the work for this thesis. In general, the dimensions or mass of a given sample is not a problem when using the VSM because the sample holder is robust and the air gap between the electromagnet can be adjusted accordingly. The VSM is fairly simple and straight forward and is based on the flux change in a copper detection coil as a magnetic sample is vibrated near it on a nonmagnetic sample rod and holder.

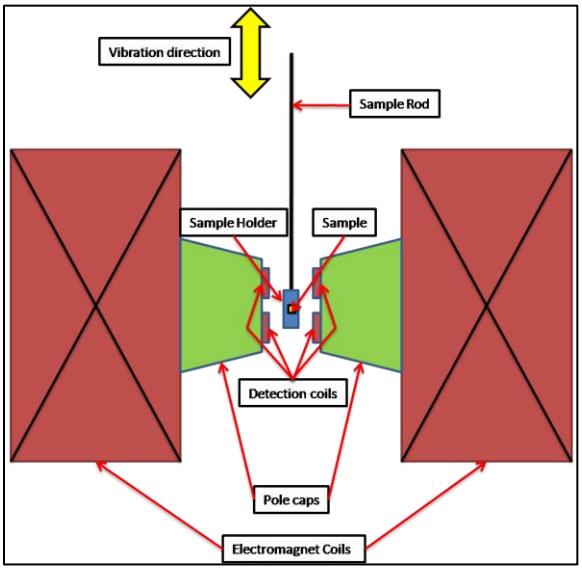

Figure 2.13: A typical set up of vibrating sample magnetometer

As a given magnetic sample is oscillated at a fixed frequency ω in an applied magnetic field $\boldsymbol{H}$ **(**in the case of the Princeton Measurement VSM it is 83 Hz) the moving sample induces an alternating electromotive force (*emf)* in the pick-up coils. The *emf is* proportional to the magnetic moment of the sample. The total flux can be written as

$$\Phi = \alpha H + \beta M sin\omega t, \tag{2.10}$$

where α and β are constants.

The induced alternating *emf* signal is very small so it is fed to a lock-in amplifier to compute *M*

$$\frac{\partial \Phi}{\partial t} = -\beta M cos\omega t. \tag{2.11}$$

The above example of the VSM is one of several different possible set ups, but all involve balanced pairs of coils that act as signal canceling agents to the applied field. The VSM used throughout this thesis research was the Princeton Measurement Corporation VSM.

2.1.5 *Alternating Gradient Magnetometer*

The Alternating Gradient Magnetometer [53] (AGM) has attributes and capabilities which can attain higher sensitivity and speed than the VSM. The minimum magnetic moment of the AGM is on the order of ~10^{-6} emu, a full order of magnitude smaller than the VSM.

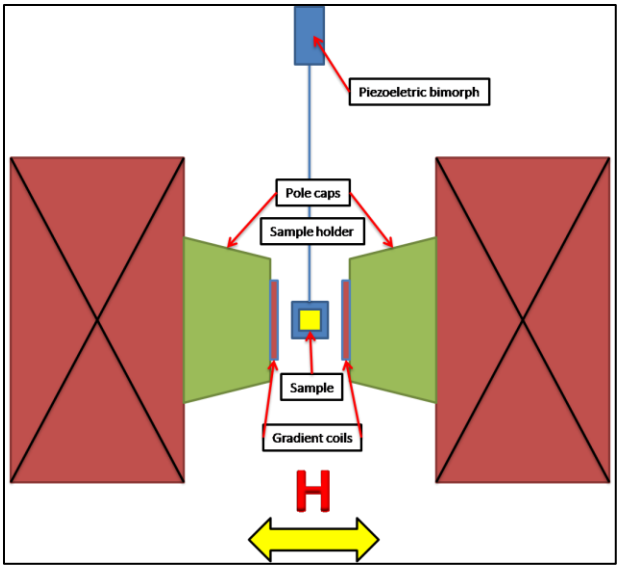

Figure 2.14: A typical set up of the alternating gradient magnetometer.

The AGM characterization method is similar to that of the VSM. Instead of using a drive motor or some other mechanical source to vibrate the sample, the AGM uses gradient coils to produce an alternating gradient field. The field gradient produces a force on the sample, which causes it to oscillate. This in turn produces stresses in the piezoelectric fiber. The piezoelectric crystal fiber generates a voltage that is proportional to the vibrational amplitude, which is proportional the sample's magnetic moment. The signal generated by the piezoelectric element is dramatically enhanced by operating at or close to the mechanical resonant frequency assembly. Commercial AGMs generally have built-in software that can automatically determine the mechanical resonance and set the appropriate frequency for a given sample.

While the AGM is more sensitive it has a few drawbacks that must considered. Since the AGM is depends on the vibration amplitude of the crystal it is susceptible to acoustic noise. Depending on the environment, it could be worth building or purchasing a sound proof booth to improve results. In addition, since the mechanical resonant frequency is mass dependant, the sample should not be too massive, about 200mg at most.

Chapter 3: *Interactions and Field-Reversal Memory in Complex Nanowire Arrays*

3.1 *Introduction*

One of the most important effects in magnetic nanowire arrays is the interwire magnetostatic interactions [51, 54-57] The interwire interaction significantly affects magnetic properties of magnetic nanowire including magnetization switching, [54, 58] microwave, [54, 59] and magnetotransport properties [43, 60]. Consequently, in order to understand the obtained experimental results, reliable methods for evaluation of interactions are needed. To quantify the effect of interactions one needs both a suitable method to experimentally vary the strength of interactions in arrays of magnetic nanowires and a method to measure the effect of the interactions.

More complex magnetization curves, such as the first order reversal curve (FORC) method, can give additional information that can be used for magnetic interaction characterization. In the case of magnetic nanowire arrays, Spinu *et al*. [61] proposed for the first time the FORC method as an effective method for magnetic interaction characterization with many other reports following.[62-68] In the majority of these reports the FORC method was used mostly as a qualitative tool to picture the existence of interaction and coercive distributions without a comprehensive quantitative analysis of magnetic interactions. One of the reasons for this situation was the lack of a series of samples with tuned interaction strengths and predetermined morphological parameters that can facilitate a correct and coherent interpretation of the wealth of information provided by the FORC measurements via theoretical models. In fact, one of the advantages of using templates for magnetic system fabrication is the possibility of obtaining model systems that can be used to test the validity of theoretical models. As the

quality of materials is dependent on the morphology of the templates, an accurate interpretation of the experimental results is difficult, especially for templates with a large geometric variability such as is the case of commercially available templates used exclusively on all previous FORC studies on magnetic nanowire arrays.

In this study, by a combined sample design and experimental measurements approach we quantitatively analyze the effect of magnetic interactions and investigate the magnetization reversal in highly ordered magnetic nanowire arrays. The magnetic nanowires were grown in highly ordered anodic alumina membranes for which the spatial distribution of the pores was controlled by a sequential application of mild and hard anodization technique [52]. Several series of samples were considered including simple wires of different lengths and diameters (70 and 110 nm) and complex wires with a single modulated diameter along their length. The FORC method was used to quantify the effect of magnetic interactions in the series of magnetic nanowire arrays. Besides the qualitative investigation of FORC diagrams, more subtle features of magnetic interactions in complex wires are revealed through a quantitative analysis of the profile of the local interaction field distributions. In addition, the FORC analyses indicate that the nanowire systems with a mean diameter of 70 nm appear to be organized in symmetric clusters indicative of a reversal-field memory effect [69].

3.2 *EXPERIMENTAL*

3.2.1 *Sample Synthesis*

To prepare more complex membranes with larger interpore distances, the same anodization procedure as described in chapter 2 was carried out, but with an additional anodization step (hard condition) at 100 V for 30 min at 5 ^{o}C to produce the mild-hard

(Mi-Ha) AAO. After the second or third anodization steps, templates were detached from the Al film by an electrochemical treatment in a 1:1 mixture solution of perchloric acid-ethanol at 100 V at 10 ^{o}C. The samples were then rinsed with distilled water and acetone. To completely remove the barrier layers, samples were immersed in a 5 wt% phosphoric acid solution. An example of such membranes prepared by multistep anodization is shown in figure 3.1. In the transition from the mild region to the hard region, approximately half of the channels remain continuous throughout the membrane while other pores initiated on the mild side terminate at the mild-hard interface. The Mi-Ha AAO can be employed as a membrane for the fabrication of the magnetic nanowire arrays. Wires were grown either in the hard or the mild side of these membranes. In the hard side of the membrane, 110-nm-diameter wires are readily obtained within all available pores. Wires fabricated in the mild side of the AAO template, however, only grow in selected pores as shown in figure 3.1. All samples were fabricated from Professor John Wiley's research group at the University of New Orleans.

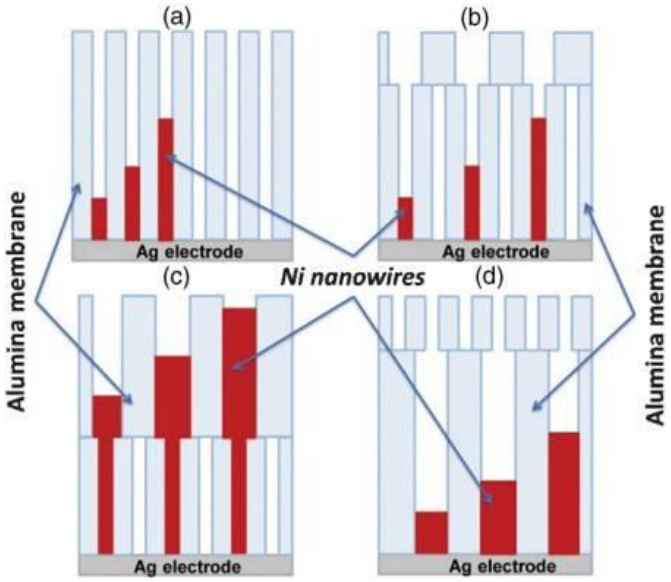

Figure 3.1: Schematic representation of the four series of samples considered (a) Mi, (b) Mi-Ha, (c) SM Mi-Ha, and (d) Ha- Mi. Each series has three samples: each sample contains nanowires of constant length, the length being different from sample to sample. The individual samples within each series are represented schematically by the three wires of different lengths in each figure, (a), (b), (c), and (d).

Ni nanowires were grown in the pores of AAO templates by electrodeposition. Initially an Ag film was sputtered onto one side of AAO template. Metal nanowires were then grown over several minutes at room temperature by a constant current method at 0.5 mA on a Princeton Applied Research VMP2 with a Pt wire counter electrode. A commercially available Ni plating solution (Technics, Inc., nickel sulfamate-RTU) was used.

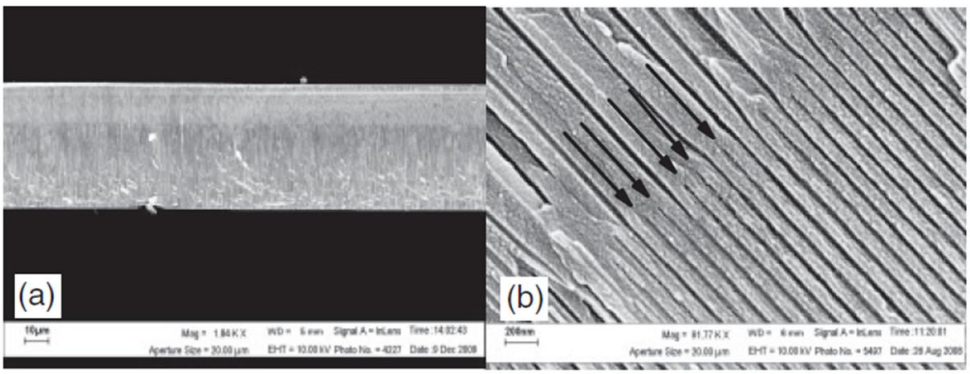

Figure 3.2: FESEM images of Mi-Ha AAO template. (a) Cross section of the boundary of mild side (top) and hard (bottom) side. (b) Higher magnification view of boundary region of mild (bottom-right) and hard side (top left); black arrows highlight some selected pores that have been terminated on the hard anodization side.

Synthesized nanostructures were characterized by field- emission scanning electron microscopy (FESEM) on a LEO1530 VP. Nanowires of different lengths were prepared by simply varying the electrodeposition time.

In this work, we have selected 4 sets of nanowire arrays for a total of 12 in order to study the effect of the diameter, the length, and the interpore distance on the magnetic properties of single-diameter nanowire arrays. Also, we studied magnetic properties of single modulated diameter nanowire arrays, where each nanowire has two different diameters. The 4 sets of samples are represented schematically in Fig. 3.1. The samples labeled mild (Mi) are array of nanowires deposited in the pores of the membrane obtained through a single-step mild anodizing

process, characterized by diameters of 70 nm, with an interpore distance of 100 nm. The mild-hard (Mi-Ha) samples are nanowires deposited only in the mild side of Mi-Ha templates. The mean diameter of the nanowires is 70 nm, and the interpore distance is about 250 nm. The hard-mild (Ha-Mi) nanowires are deposited only in the hard side of Mi-Ha templates obtaining wires with a mean diameter of 110 nm and an interwire distance of 250 nm. The single modulated (SM Mi-Ha) templates are identical to Mi-Ha and Ha-Mi, but here wires are grown such that they cross the mild and hard interface, starting from the mild side, to produce single modulated diameter structures. In this case, the portion of the nanowire from the mild side is always 14 μm in length and 70 nm in diameter, while the portion from the hard side has various lengths with a diameter of 110 nm.

3.2.2 *Magnetic measurements*

The measurements and data analysis was done following the same approach mentioned in chapter 2. Thus, the magnetic measurements (MHLs and FORCs) were done at room temperature on a Princeton AGM-VSM magnetometer (using the VSM option); this instrument is able to record a set of 100 FORCs in less than 2 h. FORC distributions were obtained by computing the mixed second-order derivative of magnetization M (H, H_R) (equation 2.1) and processed using FORCinel. In all measurements the magnetic field was applied along the length of the nanowire as shown in figure 3.3.

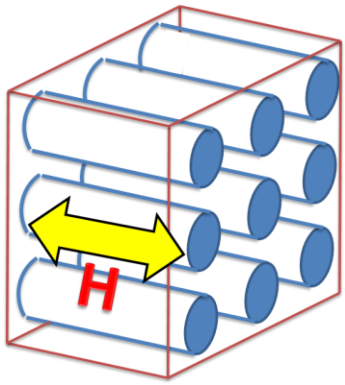

Figure 3.3: Schematic of a nanowire array with the yellow arrow indicating the applied magnetic field.

In order to quantitatively compare different FORC diagrams obtained for different samples, a statistical analysis was carried out of the profiles of both interaction and coercive field distributions. Hence, the distribution parameters as mean-field values of coercive, $<H_c>$, and interaction, $<H_u>$, fields and their corresponding standard deviations, σ_{Hc} and σ_{Hu}, were obtained. The parameters for all samples considered in this study are given in table 3.1.

A typical family of FORCs is shown in the vertical back panel of figure 3.4 for the Mi-Ha 4.8-μm sample (70-nm-diameter nanowires, interwire distance of 250 nm, and length of 4.8 μm).

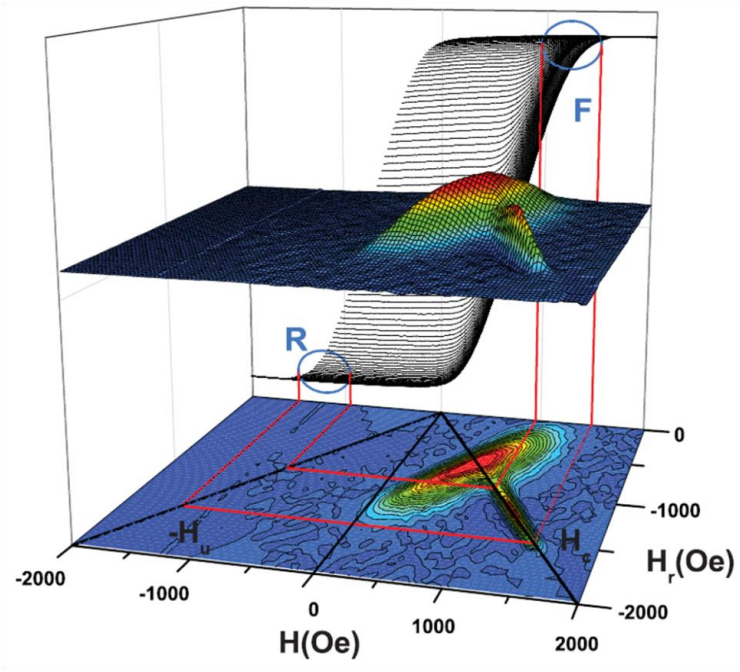

Figure 3.4: A family of FORCs from the Mi-Ha 4.8-µm nanowire array (vertical back panel), the corresponding FORC 3D distribution (top horizontal panel), and the FORC diagram (bottom horizontal panel).

The FORC distribution as a three-dimensional (3D) plot and the FORC diagram as a 2D contour plot in coordinate (H, H_R) for the Mi-Ha 4.8-µm sample are represented in the top and bottom horizontal panels of figure 3.5 respectively.

3.3 *Results and Discussion*

3.3.1 *Study of the interactions*

The main advantage of the use of the AAO templates is the fact that they allow, while keeping the same diameter distribution, the modification of the interpore distance through a controlled obstruction of the pores. In this section we study and compare the magnetic properties of the systems Mi AAO vs Mi-Ha AAO. The difference between these two systems is the average pore-pore distance. The Mi AAO systems are characterized by a nominal diameter of 70 nm, with a mean interpore distance of 100 nm, being synthesized with three different nominal

lengths: 4.0, 9.0, and 15.0 μm. The second system, Mi-Ha AAO, is characterized by the same nominal wire diameter of 70 nm, but with a mean interpore distance of about 250 nm; wires were fabricated with three different lengths: 4.8, 8.5, and 15.8 μm, respectively.

For these ranges of diameters and lengths of the mild and Mi-Ha nanowires the demagnetizing factors of the wires do not vary significantly [70] and, as expected, within the same series, Mi or Mi-Ha, The FORC diagrams do not display any noticeable variation as a function of the length of the nanowires. In figures 3.5(a) and 3.5(b) are displayed the corresponding normalized FORC diagrams for the Mi-Ha and mild nanowires with a length of 8.5 and 9.0 μm, respectively.

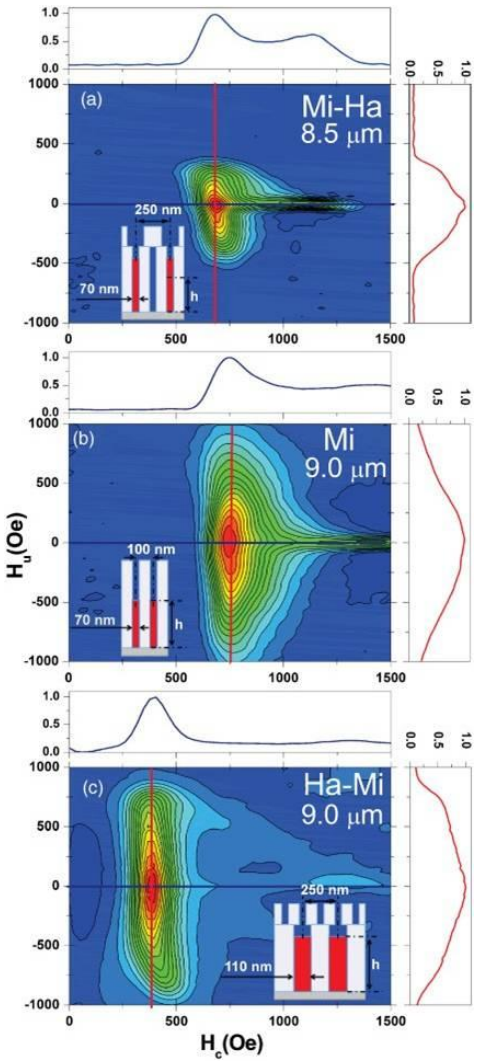

Figure 3.5: FORC diagrams of a 8.5-μm-long Mi- Ha nanowire array (a), a 9-μm-long regular Mi nanowire array (b), and a 9-μm-long Ha-Mi nanowire array (c). The top and the side insets for each figure represent the coercive field and interaction field distribution profiles obtained at the location of the horizontal (blue color online) and (red color online) vertical lines, respectively. The values of diameters and center-to-center interwire distances are given for each sample in the corresponding diagrams.

The top and the side insets represent the local coercive and interaction field distribution profiles obtained as horizontal and vertical cross sections, respectively, of the FORC distribution through its main maximum. One observes that as the interwire distance decreases the standard deviation of interaction field distribution, σ_{Hu} , increases more than two times, while the most probable value and standard deviation of coercive field distribution varies only slightly (see table

3.1). This is a clear indication of the increased effect of interwire interaction as only the distance between nanowires is decreasing. In the majority of previously published studies of interacting magnetic nanowires it was difficult to isolate and evaluate the effect of interactions when comparing different samples because more than one parameter of the assembly was varied, not just the interactions.

As shown in figure 3.5(a) and 3.5(c), by comparing the dispersion of interactions in Mi-Ha and Ha-Mi samples one observes that for the same interpore distance of 250 nm the strength of interwire interactions is larger for the Ha-Mi sample (110 nm in diameter) than for the sample Mi-Ha (70 nm).

As shown in table 3.1, one observes that the standard deviation of the local interaction field, σ_{Hu}, in all Ha-Mi samples has about the same value as in the corresponding mild samples for the three lengths considered in this study. In fact, by increasing the nanowire diameter, while the distance between their centers remains constant, the mean interaction field is also increasing, due to the closer proximity of the wires' walls [180 nm (Mi-Ha) vs 140 nm (Ha-Mi)]. Regarding the coercive field distribution of the FORC diagrams in figure 3.5, one observes a slight increase of the average coercive field value, $<H_c>$, for the mild sample relative to the Mi-Ha one while a horizontal ridge is present in the FORC diagrams of both samples. The origin of this "tail" of the FORC diagram is related to the switching mechanisms in the arrays of magnetic nanowires and is discussed in the next section.

3.3.2 *Reversal-field memory effect*

The appearance of this horizontal ridge along the coercive field axis has been reported in the literature.[62]. Béron *et al.* [62] suggested that the origin of this tail in FORC diagrams is due to a nonuniform length distribution such that, during the magnetization process, the system acts as two populations of magnetic entities. They tested this assumption by polishing the top of a wire membrane, after which the horizontal ridge in the FORC diagram disappeared. In order to verify the same hypothesis on our nanowire arrays we considered single modulated diameter Mi-Ha nanowires (SM Mi-Ha) presenting two different diameters, 70 and 110 nm. Nanowires were grown in the Mi-Ha AAO template starting from the mild side (diameter 70 nm), filling completely the mild side and continuing partially into the hard side. From Fig. 3.2(a) one observes that the separation between the mild side and the hard side is very uniform, which determines a very variation of the mild side section length of the SM Mi-Ha nanowires. The FORC diagrams of all single modulated diameter nanowire arrays display the horizontal ridge along the coercivity axis (see figure 3.6). The horizontal ridge is not the result of the larger diameter section in the composite wires because no ridge was observed for any of the samples with large diameter Ha-Mi as shown in figure 3.5. Consequently, in our case the origin of the horizontal ridge in the FORC diagram is not the result of an irregularity in the system, such as length variation, but merely an intrinsic characteristic of small-diameter nanowires.

The ridge along the coercivity axis, i.e., a wide range of coercivities with a narrow range of interactions, is in fact an additional irreversible FORC distribution located at large H_c values and very small interaction field H_u values ($H_u \cong 0$). To get a better insight into the origin of the horizontal ridge in smaller-diameter nanowire arrays we should refer to figure 3.4 where the FORC diagram is represented in the original coordinates (H,H_R), where $H = H_u + H_c$ and H_R

= $H_u - H_c$ (see chapter 2). Thus, in terms of (H,H_R) coordinates one can easily observe that the ridge is determined by switching events occurring at large values of the applied field H after the reversal field Hr ≅ −H . In figure 3.4 this property of the ridge appears evident by projecting from magnetization curves FORC regions located at $H_R \cong -H$ and H (regions delimited by the blue ellipses "R" and "F," respectively) and observing that both these projections converge on the FORC diagram ridge. In other words, the ridge is the result of switching events occurring after a reversal in the "R" region and finishing in the "F" region of the M vs H FORCs. These kinds of switching events are consistent with the "reversal-field memory" effect observed by Katzgraber *et al*. [69] in Edwards Anderson Ising spin glass (EASG) Ising-type systems. The physical origin of the reverse-field memory effect was ascribed to the existence in the magnetic system of a significant proportion of symmetric hysterons. Hysterons are independent two-state switching units that change their states from +1 to −1 and from −1 to +1 at the fields $H_u - H_c = H_R$ and Hu + Hc = H , respectively. A symmetric hysteron has a bias field $H_u = 0$ and consequently switches "symmetrically" at H and $H_R = -H$. The presence of a distribution of symmetric hysterons is evidenced by a kink in the magnetization curve, which is reflected in the FORC diagram as a ridge with its extension proportional to the range of the coercive field, H_c.

It has been claimed by some authors (e.g., Ref. [58]) that the magnetic nanowire arrays can be considered as a very good example of physical system correctly described by a classical Preisach model (also named CPM system). However, as Mayergoyz has shown in Ref. [1], the necessary and sufficient conditions to be obeyed by a CPM system are the deletion and congruency properties(see chapter 1). Systematic studies show, however, that the nanowire systems do not satisfy the congruency property. This is certainly motivated by the mean-field interactions that have to be taken into account in such systems. However, a comparison of the

parameters obtained directly from the experimental FORC distributions can be performed and may indicate with some degree of accuracy the "real" Preisach distribution characteristic to various samples. A more accurate study will include the evaluation of the influence on the results due to the state dependence of the interaction field distribution and will be presented in a future presentation.

Consequently, we consider for the moment that the nanowire systems are characterized by the Preisach distributions of hysterons P (H_c, H_u), which are identical with the experimental FORC distributions ρ (H_c, H_u). From the FORC diagrams obtained in the case of our nanowire arrays, one observes the presence of the horizontal ridge in the range of reversal-field values $-800 \leq H_R \leq -1500$ Oe for the Mi-Ha AAO nanowire arrays and in the range of $-1100 \leq H_R \leq -1700$ Oe for regular Mi AAO nanowire arrays, respectively. However, as shown in figure 3.5 for the nanowire arrays with a larger diameter, Ha-Mi, the tail of the FORC diagram is drastically diminished if not negligible. Consequently, the presence of the reversal-field memory effect in the Mi-Ha samples, with small diameter, suggests that these samples have an important number of symmetric hysterons. In contrast, the absence of the reversal-field memory effect in the Ha-Mi samples indicates that, if symmetric hysterons do exist, their proportion is not significant and the horizontal ridge in the FORC diagram is not present.

3.3.3 *Magnetic properties tuning: Complex nanowire arrays*

We have seen in the previous section that the magnetic properties of Mi-Ha AAO arrays are quite different from those of Ha-Mi AAO arrays, especially the strength of dipolar interactions. A simple way to obtain magnetic nanowire arrays with intermediate magnetic properties is to combine the Ha-Mi and Mi-Ha nanowires within the same assembly to synthesize a single modulated diameter nanowire array. The magnetic properties of these complex

nanowires can be further tuned by varying the length ratio of the two components, Mi-Ha and Ha-Mi. An exemplification of this approach is shown in figure 3.6 where the FORC diagrams of Mi-Ha 15.8-μm, Ha-Mi 15.0-μm, and modulated Mi-Ha 30-μm samples composed of two 15.0-μm-long sections of diameters 70 and 110 nm are represented.

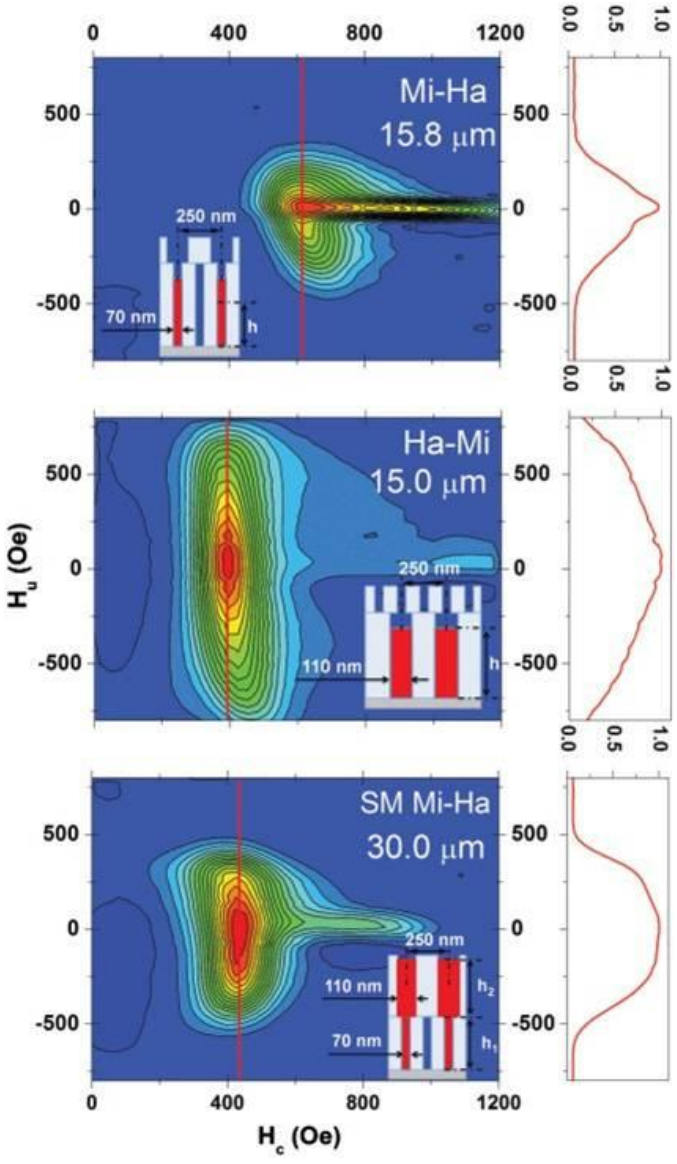

Figure 3.6: (Color online) Comparison between FORC diagrams of Mi-Ha nanowire array (top), Ha-Mi AAO nanowire array (middle), and SM Mi-Ha nanowire array with the lengths of Mi and Ha segments h_1=15μm and h_2=15μm, respectively (bottom). The right side panel displays the corresponding profile of the local interaction field distribution for each sample. The values of diameters and center-to-center interwire distances are given for each sample in the corresponding diagrams.

From the local interaction field distribution profiles shown in the right side panel one observes that the strength of dipolar interaction in the single modulated diameter nanowire array sample is intermediate between interactions in the Mi-Ha and Ha-Mi samples. Furthermore, one observes subtle differences in the way the interaction field is decaying upon moving away from the $H_u = 0$ line. Thus, in the Mi-Ha sample the dipolar interactions are localized with a quasilinear decay of the interaction field, while in the Ha-Mi sample the interaction field is broadly distributed with a convex decay. The combination of the two aforementioned effects in the single modulated diameter nanowire samples results in an intermediate width of the interaction field distribution with a localized convex decay.

The statistical analysis done on the profiles of the interaction and coercive field distributions for all samples allows us to better assess and summarize these differences between samples from the three different series. For the sake of consistency the coercive field profiles $\rho(H_c)$ were fitted for all samples with a double-peak Gaussian distribution,

$$\rho(H_c) = \sum_{i=1,2} A_i \, e^{\left[\frac{-\left(H_c - \langle H_{c,i} \rangle\right)}{2\sigma^2_{Hc,1}}\right]} \tag{3.1}$$

allowing determination of the average values $\langle H_{c1} \rangle$ and $\langle H_{c2} \rangle$ of the coercive field for both peaks and their corresponding standard deviations σ_{Hc1} and σ_{Hc2} . The same procedure was applied to the interaction field profiles $\rho(H_u)$ taken for each sample at $H_c = \langle H_{c1} \rangle$ and $H_c = \langle H_{c2} \rangle$. Using the standard deviations of the coercive and interaction field distributions for both peaks one can calculate $m_1/(m_1 + m_2)$, the ratio between the magnetic moment associated with the lower coercivity peak, m_1 , and the total magnetic moment m_1+m_2 . As shown in table 3.1, $m_1 / (m_1 + m_2)$ is very close to 100% for all Ha-Mi samples with large diameter (110 nm).

Sample	$\langle H_{c1} \rangle$ (Oe)	$\sigma_{Hc1}(Oe)$	$\langle H_u \rangle$ (Oe)	σ_{Hu} (Oe)	$\langle H_{c2} \rangle$ (Oe)	σ_{Hc2} (Oe)	$m_1/(m_1+m_2)$ (%)
Mi 4-μm	714	86	1	499	1302	465	86.0
Mi 9-μm	764	87	−49	498	1313	358	85.5
Mi 15-μm	740	79	−6	416	1261	389	82.5
Mi-Ha 4.8−μm	670	87	−35	277	1090	200	83.0
Mi-Ha 8.5−μm	720	92	−15	209	1080	181	79.9
Mi-Ha 15.8−μm	617	77	−17	182	933	193	62.2
Ha-Mi 4-μm	390	77	17	438	1259	117	98.1
Ha-Mi 9-μm	390	70	16	548	1288	141	97.4
Ha-Mi 15-μm	400	72	27	460	1144	171	96.5
Mi-Ha (14 + 5)-μm	488	74	−19	350	860	204	92.8
Mi-Ha (14 + 10)-μm	482	75	−29	340	867	210	91.8
Mi-Ha (14 + 16)-μm	436	80	−23	309	766	146	90.4

Table 3.1: Statistical analysis of the FORC distributions.

For smaller-diameter samples (Mi and Mi-Ha) the second FORC distribution peak is more noticeable as attested by smaller values of $m_1 / (m_1 + m_2)$. Essentially, for these samples the second distribution peak is part of the reversal-field memory ridge discussed in the previous section, but depending on the interaction strength, one observes subtle differences. For Mi-Ha samples with weak dipolar interactions the second coercivity peak is well defined, while for Mi samples with stronger interwire interactions, the peak is absorbed in the horizontal ridge (see figure 3.5). Thus, the increase of interwire interactions has as an effect a delocalization of the symmetric hysteron distribution along the coercive field H_c axis.

For a better visualization of the statistical analysis results summarized in table 3.1, we plotted in figure 3.7 the length dependency of the main statistical parameters, average coercive field, and dispersion of dipolar interaction field.

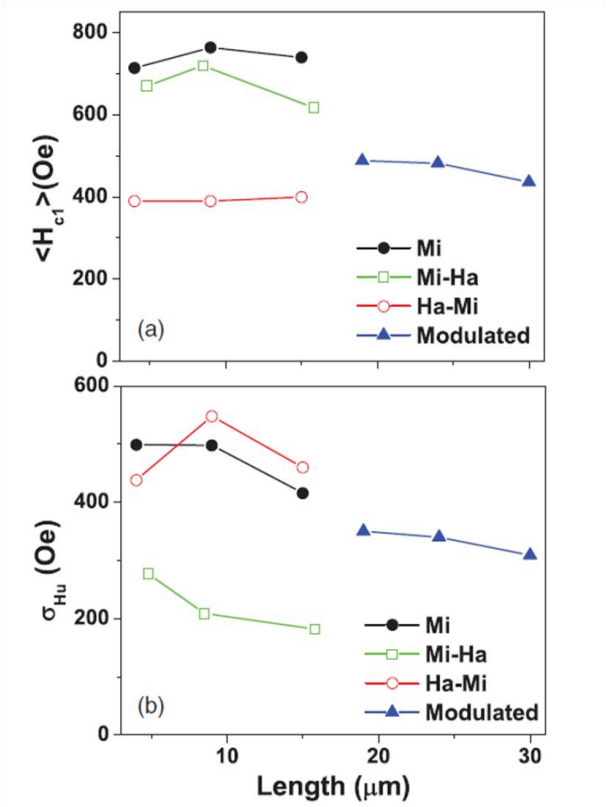

Figure 3.7: Length dependency of (a) the mean value of the main coercive field and (b) the standard deviation of the main interaction field distribution.

One observes that for all series the average coercive field does not vary significantly with the length of nanowire within this length range. By increasing the wire diameter one observes a variation of the coercive field mean value from about 750 Oe, for a nanowire diameter of 70 nm (Mi samples), down to 400 Oe, for a diameter of 110 nm (Ha-Mi samples). This is consistent with a variation of the coercive field inverse proportional with the diameter previously observed in similar systems [71] and associated with a noncoherent magnetization reversal in the case of magnetic nanowires with diameters larger than the critical diameter D_{coh} which for Ni is 26 nm [72-74] From the σ_{Hu} vs. wire-length plot, it clearly appears that the strength of interactions in complex nanowires is intermediate between the interactions in Mi-Ha and Ha-Mi samples, as discussed previously. Furthermore, by increasing wire diameters it is possible to strengthen the

dipolar interactions arriving at the point that thick Ha-Mi wires have essentially the same value of the standard deviation of the interaction field as thin Mi wires. As the wire diameter is proven to be efficient for changing both the standard deviation of the interaction field distribution and the average wire coercivity, it is interesting to observe the properties of complex wires (thin + thick). The results show that these wires provide average values for both coercivity and interaction intensity, which is another essential tool to obtain systems with tailored properties.

3.4 *Conclusions*

We have systematically studied the dipolar interaction effects and reversal behavior in highly ordered magnetic nanowire arrays by a combination of sample design and fabrication and magnetic measurements using the FORC method. Taking advantage of high-quality AAO templates obtained through a sequential application of mild and hard anodization techniques we were able to include in our study four different series of nanowire samples with good control of diameter, interwire spacing, and complexity (simple and single modulated diameter wires). The effect of dipolar interactions was studied by considering samples with virtually identical diameter distributions but different interwire distances as provided by a controlled obstruction of the pores of the AAO templates. This is essential for a correct evaluation of the effect of the interactions in magnetic nanowire arrays, as it is well-known that nanowire arrays with different diameters are subject to different strengths of interaction. Utilizing the FORC technique and through a quantitative analysis of the profiles of local interaction and coercive field distributions a detailed description of the magnetic interactions and magnetization reversal was obtained. Thus, for the Mi-Ha series with nanowires of 70-nm diameter and 250-nm interwire distance, the strength of dipolar interactions was significantly reduced relative to nanowires from Mi series having the same diameter but a 100-nm interwire distance. In addition FORC analysis indicates

that the nanowire systems with a mean diameter of 70 nm seem to be organized in symmetric clusters indicative of a reversal-field memory effect. The increase of interwire interactions enhances the reversal-field memory effect as reflected by a delocalization of the symmetric hysteron distribution toward higher coercive field values for the Mi samples. The Ha-Mi series, including thick wires of 110 nm in diameter and the same wire center-to-center distance as the Mi-Ha series (250 nm), displayed an enhanced strength of interactions as in the case of the Mi series. The composite Mi-Ha series composed of single modulated wires (70 and 110 nm) allowed us to obtain magnetic properties intermediate to those of simple thin and thick wires. Moreover, one observes subtle differences in the profiles of interaction field distributions. Thus, in the Mi-Ha sample the dipolar interactions are localized with a quasilinear decay of the interaction field, while in the Ha-Mi sample the interaction field is broadly distributed with a convex decay. The combination of the two aforementioned effects in the single modulated diameter nanowire samples results in an intermediate width of the interaction field distribution with a localized convex decay. Thus, by a careful choice of methods of preparing high-quality templates one can obtain complex magnetic nanowire systems with tunable magnetic properties. Furthermore, this study confirms that the FORC method is an effective tool for studying interactions and reversal properties of magnetic nanowire arrays.

Chapter 4: *FORC analysis of FeCoB/Ru/FeCoB Synthetic Antiferromagnets*

4.1 *Introduction*

Synthetic antiferromagnets (SAF) consist of two thin ferromagnetic films with moments of the same (or different) magnitude, strongly coupled antiferromagnetically due to the Ruderman-Kittel-Kasuya-Yosida (RKKY) interaction through an ultrathin spacer layer, typically Ru, 0.6 − 0.9 nm thick[75, 76].To enhance the interlayer coupling in SAF materials, a trilayer film of boron-added FeCo alloys, with Ru as separator layer, have showed very promising properties because of their large saturation magnetization simultaneous with a soft magnetic response [77]. Examples range from pinned to free layers in MRAM and magnetic sensors. The switching properties of the SAF structures dictate the performance of these technological devices. Therefore, the study of their properties is important to both technological and scientific points of view [78, 79].

In 2006, Hashimoto *et al.* [77] reported on the extremely large flopping and saturation fields for FeCoB/Ru/FeCoB, where the Ru thickness was systematically changed from 0nm to 4nm. Using basic analysis of the major hysteresis loops, the exponential decay-oscillatory trends of the flopping field and saturation field were examined. It was claimed that the large bilinear coupling generated due to the suppression of ferromagnetic coupling, interfacial smoothness, and the shift to the first peak caused by the RKKY-like interlayer coupling for small Ru thicknesses.

Radu *et al.* [80] also studied the SAF system of FeCoB/Ru/FeCoB, where the Ru thickness was changed from 0 nm to 2 nm. With a different switching field distribution, they

proved that through the angular variation of the magnetic susceptibility it is possible to build up a switching field vector diagram, in analogy with the well-known astroid from the coherent rotation model for uniaxial anisotropy. In particular, it was hown that that the critical curve could be considered the fingerprint of the switching behavior and provides information about micro-magnetic and structural properties of the SAF, an essential component of modern magnetic devices as memories and sensors [81].

Interestingly, due to the fast drop of the oscillatory strength of the ferromagnetic coupling between the magnetic layers as the interlayer thickness is increased, the oscillatory strength seems to be negligible for thicker interlayers above 2 nm thicknesses. For example, Yuan-Jen Lee *et al*., theoretically studied the oscillatory behavior for long-range exchange bias in ferromagnet and antiferromagnet layers separated by a nonmagnetic metal spacer [82, 83].

In the last 10 years, with the subsequent improvements in experimental techniques, in particular related to the vibrating sample magnetometry (VSM), First Order Reversal Curve (FORC) diagrams opened a new possibility to reliably quantify and map the interplay between the internal fields and interactions in SAF systems [84, 85]. FORC diagrams have proved to be highly adequate characterization tools for the quantitative analysis of many magnetic systems with different interaction and coupling geometries[26, 64, 85, 86].

In this research a series of SAF samples provided by Dr. Ganping Ju from Seagate was examined by using FORC diagrams. Their structure has consisted of FeCOB/Ru/FeCoB trilayers, with the Ru interlayer varying from the nominal distances of 1.2 nm, 1.4 nm, 1.6 nm and 1.8 nm. As discussed in [77], for this range of Ru film thicknesses, the second most important maxima on the oscillatory dependence of the flopping and saturation fields is included.

This work explores the basic SAF structure with only two ferromagnetic layers separated by a nonmagnetic metallic interlayer. FORC diagrams can be used to characterize the distributions of the internal and interaction fields and to generate information that can be useful in understanding the basic mechanism of the switching field magnetization [87].

4.2 *Experimental*

The samples under study were SAF structures of type FeCoB/Ru/FeCoB with a carbon overcoat layer provided by Dr. Ganping Ju from Seagate. The layers were deposited at room temperature using a dc magnetron sputtering with a base vacuum pressure below $3x10^{-9}$ Pa. SAF samples were grown with nominal 20 nm thickness for the ferromagnetic FeCoB layers and a Ru interlayer nominal thickness of 1.6 nm and 1.8 nm. Each sample was cut in the radial direction from a disc to make a 5mm x 5mm square. The relative Fe/Co ratio was determined by Energy Dispersive Spectroscopy (EDS); an average value of Fe/Co=1.35 was obtained. The crystal structure of the SAF samples were analyzed by using a Cu-kα X-ray Powder Rigaku diffractometer (XRD, λ = 0.15418 nm).

All FORC measurements were performed at room temperature with a Princeton Measurements vibrating sample magnetometer (VSM), with a sensitivity of 0.5 μemu at 1 sec per point. This allowed more than 100 FORC curves in to be obtained less than 1 h.

4.3 *FORC analysis and interpretation*

The switching field distributions (SFD) were determined for each sample using equation (2.7) and described in chapter 2. By obtaining the SFD the start and finish of irreversible behavior was determined.

4.4 *Results and discussion*

The inset in Figure 4.1is a typical XRD pattern of sample R-18, where the crystalline peaks for FeCo (110) and FeCo (200), Ru (002), and the stronger peak of the C (200) are marked. The weak intensity and broadening of the FeCo peaks can be explained due to Boron inclusion on these samples, suggesting a polycrystalline structure for these FeCoB alloys. Fig. 4.1-bottom shows the EDS for the same sample R-18, where it is possible to see the contributions of the main elements Fe and Co, with iron-rich concentration, and average value of Fe/Co = 1.35.

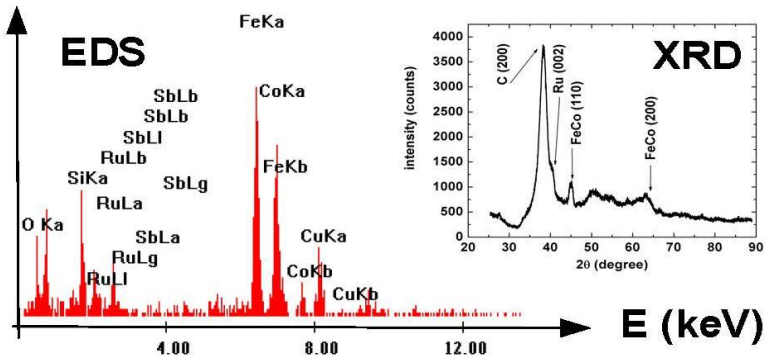

Figure 4.1: The inset corresponds to the typical X-ray diffraction pattern XRD for sample R18. EDS for the same sample R18, where it is possible to detect the contributions of the main elements Fe and Co, with iron-rich concentration, average value of Fe/Co = 1.35.

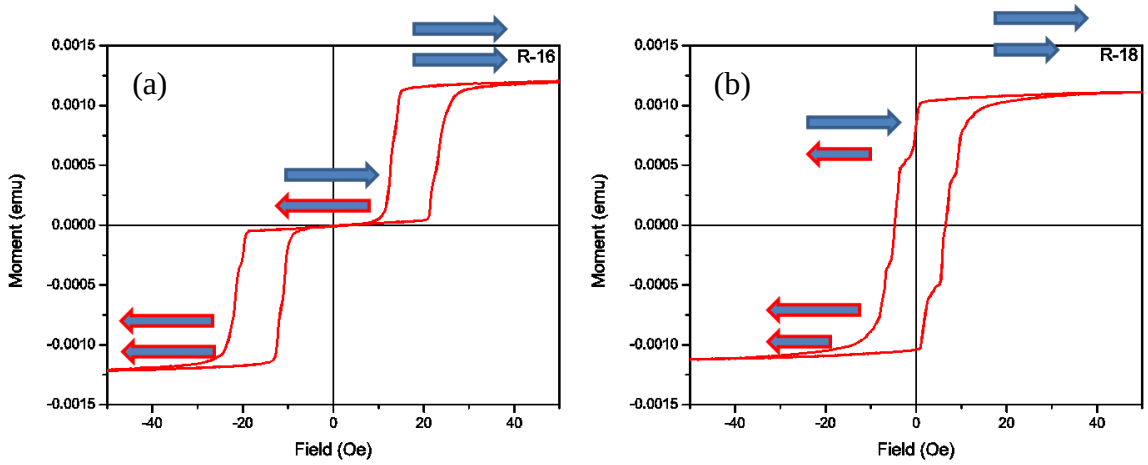

Figure 4.2: MHL for R-16(a) shows symmetric layer switching and R-18(b) shows asymmetric layer switching.

In figure 4.2(a) the switching mechanism for R-16 is a product of the symmetric ferromagnetic FeCoB layers. Beginning at a positive saturation magnetization, upon the removal of the applied field the layers will return to a lower energy state of anti-ferromagnetic behavior. Continuing to negative saturation magnetization and cycling back to positive reveals "splitting" of the MHL into two anti-symmetric loops, which was what was to be expected. From the magnetization data shown in figure 4.2(b) the behavior for R-18 is quite different and the mgnetization switching in this case may be associated with non symmetric SAF structure. as schematically indicated by the arrows in figure 4.2(b).

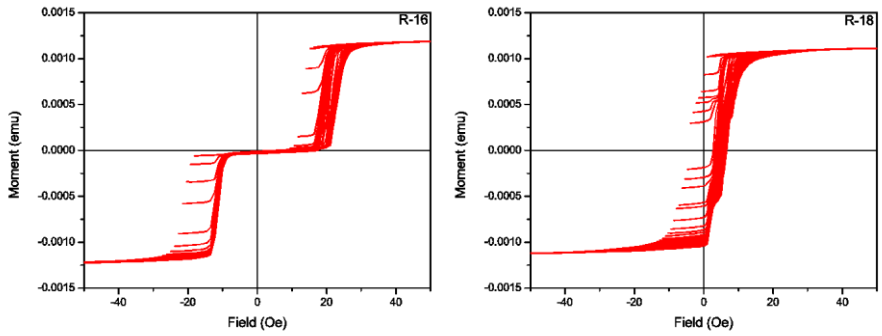

Figure: 4.3FORC curves for R-16 (left) and R-18 (right).

From the calculated FORC curves in figure 4.3 we obtained the associated FORC distributions (figure 4.4). The 2-D FORC distribution for R-16 (figure 4.4(a)) reveals three well defined distributions due to the SAF coupling. The positive and negative destitutions come from the top and bottom loops in figure 4.2 (a) respectively. The third distribution located on the H_c axis that appears R-16's 2-D contour plot is a memory effect from a "kink" in the FORC toward the front of the positive loop that originates from a negative reversal field close to negative

saturation [88] which is an indication of the coupling between the ferromagnetic layers. This is better viewed in figure 4.5.

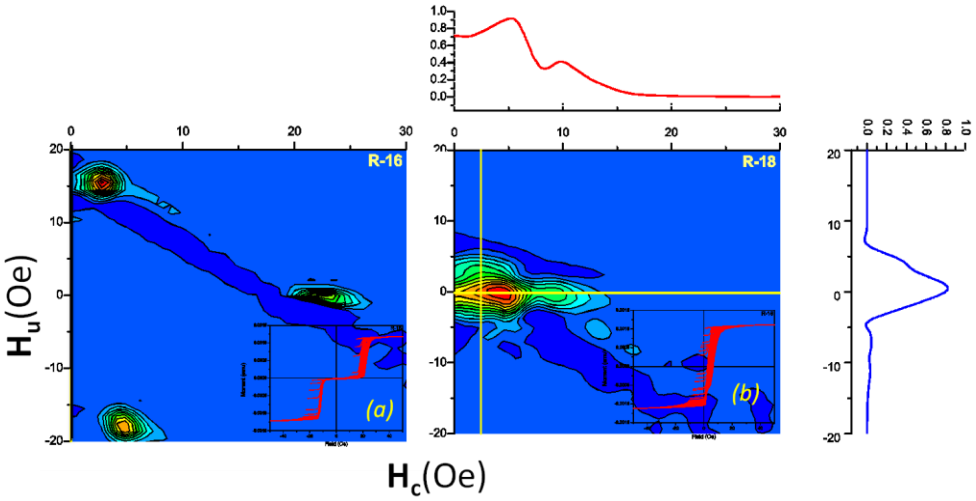

Figure: 4.4: FORC couture plot of R-16(a) and R-18(b).

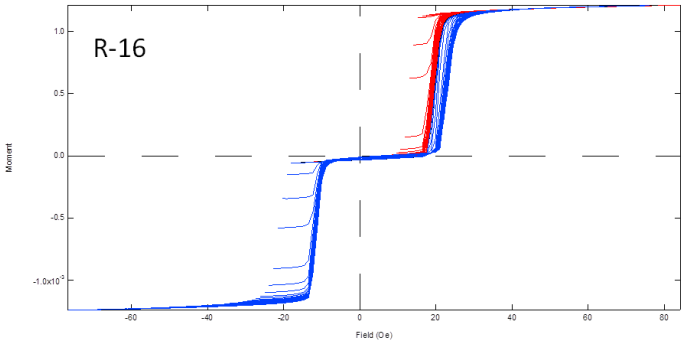

Figure 4.5: Colorized FORCs of R-16.

The red and blue FORCs in figure 4.5 contribute to the positive and negative FORC distributions in figure 4.4(a) and 4.4(b) respectively. While the MHL indicates that the ferromagnetic layers in R-16 are symmetric, further analysis of the FORC reveals that the positive and negative distributions are not completely identical. This behavior can be related to the inhomogeneities of the ferromagnetic layers thicknesses. These results can be better viewed in table 4.1 where the parameters obtained from a statistical analysis of the FORC distributions are presented

R-16	$\langle H_c \rangle$	$\langle \sigma_c \rangle$	$\langle H_u \rangle$	$\langle \sigma_u \rangle$
D_{up}	3.5	2.21	16.4	2.04
D_{down}	5.51	1.98	-18.5	4.84
D_{center}	23.1	3.8	0.2	1.0
R-18	$\langle H_c \rangle$	$\langle \sigma_c \rangle$	$\langle H_u \rangle$	$\langle \sigma_u \rangle$
D_{up}	----	----	----	----
D_{down}	----	----	----	----
D_{center}	4.66	2.92	2.26	3.9

Table 4.1: Statistical analysis of the profile distributions of R-16 and R-18

The FORC distribution of R-18 (figure 4.4(b)) is a single distribution with a "tail" along H_c which is similar to the memory effect described for R-16. Focusing on the right profile in figure 4.4(b), the appearance of a shoulder indicates the switching of the thinner ferromagnetic layer while the main peak is the thicker layer.

Figure 4.6 shows FORC-SFD, obtained by the integration of the FORC distribution along the H axis. The SFD for R-18 is a single Gaussian-like distribution in good agreement with the FORC distribution in H/H_r coordinates. The SFD for R-16 shows two narrow peaks, as expected when compared to the corresponding FORC distribution.

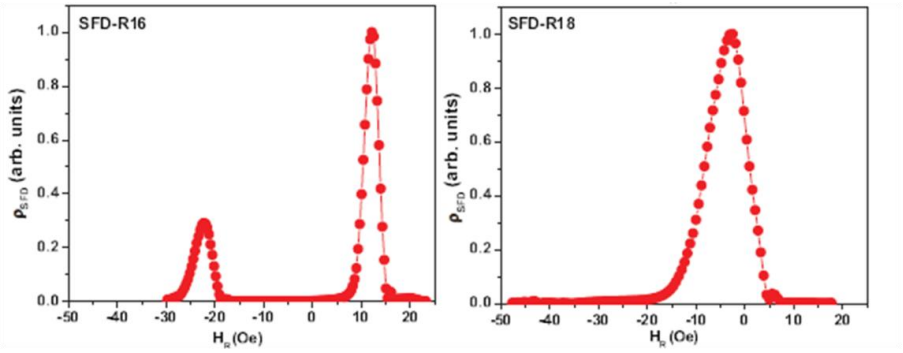

Figure 4.6: The FORC-switching field distribution (SFD), obtained by the integration of the FORC distribution along the H axis: R16 (1.6 nm Ru separator layer), and R18 (1.8 nm Ru separator layer).

4.5 *Conclusions*

A different method was used to characterize the irreversible magnetization switching process in synthetic-antiferromagnetic structures. A series of samples were examined by the First Order Reversal Curve (FORC) method where the structure consisted of FeCOB/Ru/FeCoB trilayers. The Ru interlayer thickness values of 1.6 nm and 1.8 nm. The FORC analysis identifies and quantifies the strength of the internal field interactions. To gain better insight of the magnetic behaviors, the switching field distribution (SFD) was determined to quantify the internal field distributions. Therefore, this type of information is related to the anti-ferromagnetic coupling of the layers and gives insight into the nature and strength of the coupling between the ferromagnetic layers. In addition, view its under 1 Oe resolution the FORC method was able to reveal very small differences in magnetization switching of the ferromagnetic layers detecting layer inconsistencies and furthering that it is a power characterization tool.

References

1. Mayergoy, I.D., *Mathematical Models of Hysteresis and Their Applications*, *Elsevier Series in Electromagnetism*. 1st ed2003.
2. Cullity, B.D., Graham, C.D., *Introduction to Magnetic Material*. Second ed2009: John Wiley & Sons, Inc.
3. Chikazumi, S., *Physics of Ferromagnetism*. 2nd ed1997: Oxford: Clarendon.
4. Jiles, D., *Introduction to Magnetism and Magnetic Materials*. Second ed1998: Taylor & Francis.
5. Kittel, C., *Introduction to Solid State Physics*. Eighth ed2005: John Wiley & Sons, Inc.
6. Stoner, E.C. and E.P. Wohlfarth, *A MECHANISM OF MAGNETIC HYSTERESIS IN HETEROGENEOUS ALLOYS (REPRINTED FROM PHILOSOPHICAL TRANSACTION ROYAL SOCIETY-LONDON, VOL 240, PG 599-642, 1948).* Ieee Transactions on Magnetics, 1991. **27**(4): p. 3475-3518.
7. Tannous, C. and J. Gieraltowski, *The \Stoner-Wohlfarth model of ferromagnetism.* European Journal of Physics, 2008. **29**(3): p. 475-487.
8. Wernsdorfer, W., et al., *Experimental evidence of the Neel-Brown model of magnetization reversal.* Physical Review Letters, 1997. **78**(9): p. 1791-1794.
9. L. Neel, A., Goephys, 1949. **5**: p. 99.
10. Brown, W.F., Physical Review Letters, 1963. **130**: p. 1677.
11. Bean, C.P. and J.M. Livingston, *Superparamagnetism.* Journal of Applied Physics, 1959. **30**: p. 120S.
12. Knobel, M., et al., *Superparamagnetism and Other Magnetic Features in Granular Materials: A Review on Ideal and Real Systems.* Nanoscience and Nanotechnology, 2008. **8**: p. 2836–2857.
13. Preisach, F., Z. Phys, 1935. **94**: p. 277.
14. Sorop, T.G., et al., *Magnetization reversal of ferromagnetic nanowires studied by magnetic force microscopy.* Physical Review B, 2003. **67**(1).
15. Mayergoyz, I.D., IEEE Trans. Magn. **22**: p. 603.
16. Rotaru, A., et al., *Interactions and reversal-field memory in complex magnetic nanowire arrays.* Physical Review B, 2011. **84**(13).
17. Hwang, M., et al., *Major hysteresis loop modeling of two-dimensional arrays of single domain particles.* Ieee Transactions on Magnetics, 2000. **36**(5): p. 3173-3175.
18. Bahiana, M., et al., *Reversal modes in arrays of interacting magnetic Ni nanowires: Monte Carlo simulations and scaling technique.* Physical Review B, 2006. **74**(17): p. 174412.
19. Bertotti, G., *Hysteresis in Magnetism: For Physicists, Materials Scientists, and Engineers, Electromagnetism*1998, San Diego: Academic Press.
20. I. D. Mayergoyz, *Mathematical Models of Hysteresis and Their Applications, Elsevier Series in Electromagnetism,* . 1th ed2003, Elsevier, Amsterdam/Boston.
21. Spratt, G.W.D., et al., *STATIC AND DYNAMIC EXPERIMENTAL STUDIES OF PARTICULATE RECORDING MEDIA.* Journal of Magnetism and Magnetic Materials, 1988. **75**(3): p. 309-318.
22. Kelly, P.E., et al., *Switching mechanisms in cobalt-phosphorus thin films.* Magnetics, IEEE Transactions on, 1989. **25**(5): p. 3881-3883.
23. Pike, C.R., A.P. Roberts, and K.L. Verosub, *Characterizing interactions in fine magnetic particle systems using first order reversal curves.* Journal of Applied Physics, 1999. **85**(9): p. 6660-6667.

24. Roberts, A.P., C.R. Pike, and K.L. Verosub, *First-order reversal curve diagrams: A new tool for characterizing the magnetic properties of natural samples.* Journal of Geophysical Research-Solid Earth, 2000. **105**(B12): p. 28461-28475.
25. Davies, J.E., et al., *Magnetization reversal of Co/Pt multilayers: Microscopic origin of high-field magnetic irreversibility.* Physical Review B, 2004. **70**(22): p. 224434.
26. Spinu, L., et al., *Method for magnetic characterization of nanowire structures.* Ieee Transactions on Magnetics, 2004. **40**(4): p. 2116-2118.
27. Davies, J.E., et al., *Anisotropy dependence of irreversible switching in Fe/SmCo and FeNi/FePt exchange spring magnet films.* Applied Physics Letters, 2005. **86**(26).
28. Davies, J.E., et al., *Magnetization reversal and nanoscopic magnetic-phase separation in La_{1−x}Sr_{x}CoO_{3}.* Physical Review B, 2005. **72**(13): p. 134419.
29. Pike, C.R., et al., *First-order reversal curve diagram analysis of a perpendicular nickel nanopillar array.* Physical Review B, 2005. **71**(13): p. 134407.
30. Katzgraber, H.G., et al., *Finite versus zero-temperature hysteretic behavior of spin glasses: Experiment and theory.* Physical Review B, 2007. **76**(9): p. 092408.
31. Dumas, R.K., et al., *Magnetic fingerprints of sub-100nm Fe dots.* Physical Review B, 2007. **75**(13): p. 134405.
32. Stancu, A., et al., *First-order reversal curves diagrams for the characterization of ferroelectric switching.* Applied Physics Letters, 2003. **83**(18): p. 3767-3769.
33. Ramírez, J.G., et al., *First-order reversal curve measurements of the metal-insulator transition in VO_{2}: Signatures of persistent metallic domains.* Physical Review B, 2009. **79**(23): p. 235110.
34. Tanasa, R., et al., *First-order reversal curve analysis of spin-transition thermal hysteresis in terms of physical-parameter distributions and their correlations.* Physical Review B, 2005. **71**(1): p. 014431.
35. Enachescu, C., et al., *First-order reversal curves analysis of rate-dependent hysteresis: The example of light-induced thermal hysteresis in a spin-crossover solid.* Physical Review B, 2005. **72**(5): p. 054413.
36. Dîrtu, M.M., et al., *Insights into the Origin of Cooperative Effects in the Spin Transition of [Fe(NH2trz)3](NO3)2: the Role of Supramolecular Interactions Evidenced in the Crystal Structure of [Cu(NH2trz)3](NO3)2·H2O.* Inorganic Chemistry, 2010. **49**(12): p. 5723-5736.
37. Rotaru, A., et al., *Pressure effect investigated with first-order reversal-curve method on the spin-transition compounds [Fe_{x}Zn_{1-x}(btr)_{2}(NCS)_{2}] · H_{2}O (x=0.6,1).* Physical Review B, 2011. **83**(22): p. 224107.
38. Harrison, R.J. and J.M. Feinberg, *FORCinel: An improved algorithm for calculating first-order reversal curve distributions using locally weighted regression smoothing.* Geochemistry Geophysics Geosystems, 2008. **9**.
39. Fert, A. and L. Piraux, *Magnetic nanowires.* Journal of Magnetism and Magnetic Materials, 1999. **200**(1-3): p. 338-358.
40. Skomski, R., *Nanomagnetics.* Journal of Physics-Condensed Matter, 2003. **15**(20): p. R841-R896.
41. Sellmyer, D.J., M. Zheng, and R. Skomski, *Magnetism of Fe, Co and Ni nanowires in self-assembled arrays.* Journal of Physics-Condensed Matter, 2001. **13**(25): p. R433-R460.
42. Ye, B., et al., *Passive high-frequency devices based on superlattice ferromagnetic nanowires.* Journal of Magnetism and Magnetic Materials, 2007. **316**(2): p. E56-E58.
43. Mourachkine, A., et al., *Template Nanowires for Spintronics Applications: Nanomagnet Microwave Resonators Functioning in Zero Applied Magnetic Field.* Nano Letters, 2008. **8**(11): p. 3683-3687.
44. Huynen, I., et al., *A novel nanostructured microstrip device for tunable stopband filtering applications at microwaves.* Ieee Microwave and Guided Wave Letters, 1999. **9**(10): p. 401-403.

45. Dubois, S., et al., *Perpendicular giant magnetoresistance of NiFe/Cu multilayered nanowires.* Applied Physics Letters, 1997. **70**(3): p. 396-398.
46. Maurer, T., et al., *Magnetic nanowires as permanent magnet materials.* Applied Physics Letters, 2007. **91**(17).
47. Wade, T.L. and J.E. Wegrowe, *Template synthesis of nanomaterials.* European Physical Journal-Applied Physics, 2005. **29**(1): p. 3-22.
48. Martin, C.R., *Membrane-based synthesis of nanomaterials.* Chemistry of Materials, 1996. **8**(8): p. 1739-1746.
49. Fleischer, R.L., P. B. Price, and R. M. Walker, *Nuclear Tracks in Solids: Principles and Applications*1975, Berkeley: University of California Press.
50. Spohr, R., et al., *Controlled fabrication of ion track nanowires and channels.* Nuclear Instruments & Methods in Physics Research Section B-Beam Interactions with Materials and Atoms, 2010. **268**(6): p. 676-686.
51. Masuda, H. and K. Fukuda, *ORDERED METAL NANOHOLE ARRAYS MADE BY A 2-STEP REPLICATION OF HONEYCOMB STRUCTURES OF ANODIC ALUMINA.* Science, 1995. **268**(5216): p. 1466-1468.
52. Lim, J.H., et al., *Synthesis of mild-hard AAO templates for studying magnetic interactions between metal nanowires.* Journal of Materials Chemistry, 2010. **20**(41): p. 9246-9252.
53. Flanders, P.J., *An alternating‐gradient magnetometer (invited).* Journal of Applied Physics, 1988. **63**(8): p. 3940-3945.
54. Encinas-Oropesa, A., et al., *Dipolar interactions in arrays of nickel nanowires studied by ferromagnetic resonance.* Physical Review B, 2001. **63**(10): p. 104415.
55. Dumitru, I., et al., *Study of magnetic interactions in metallic nanowire networks.* Magnetics, IEEE Transactions on, 2005. **41**(10): p. 3361-3363.
56. Trusca, O.C., et al., *Interaction Effects in Ni Nanowire Arrays.* Magnetics, IEEE Transactions on, 2008. **44**(11): p. 2730-2733.
57. De La Torre Medina, J., et al., *Double ferromagnetic resonance and configuration-dependent dipolar coupling in unsaturated arrays of bistable magnetic nanowires.* Physical Review B, 2010. **81**(14): p. 144411.
58. Sorop, T.G., et al., *Magnetization reversal of ferromagnetic nanowires studied by magnetic force microscopy.* Physical Review B, 2003. **67**(1): p. 014402.
59. Sklyuyev, A., et al., *Microwave studies of magnetic anisotropy of Co nanowire arrays.* Journal of Applied Physics, 2009. **105**(2).
60. Silva, R.A., et al., *Magnetoresistance and magnetization reversal of single Co nanowires.* Physical Review B, 2009. **79**(13): p. 134434.
61. Spinu, L., et al., *Method for magnetic characterization of nanowire structures.* Magnetics, IEEE Transactions on, 2004. **40**(4): p. 2116-2118.
62. Beron, F., et al., *First-Order Reversal Curves Diagrams of Ferromagnetic Soft Nanowire Arrays.* Magnetics, IEEE Transactions on, 2006. **42**(10): p. 3060-3062.
63. Clime, L., et al., *Characterization of ferromagnetic nanowires by partial first order reversal curves.* Journal of Applied Physics, 2007. **102**(6).
64. Beron, F., et al., *Reversible and quasireversible information in first-order reversal curve diagrams.* Journal of Applied Physics, 2007. **101**(9).
65. Beron, F., et al., *Magnetic Behavior of Ni/Cu Multilayer Nanowire Arrays Studied by First-Order Reversal Curve Diagrams.* Magnetics, IEEE Transactions on, 2008. **44**(11): p. 2745-2748.
66. Lavin, R., et al., *Magnetic Characterization of Nanowire Arrays Using First Order Reversal Curves.* Magnetics, IEEE Transactions on, 2008. **44**(11): p. 2808-2811.

67. Ciureanu, M., et al., *First Order Reversal Curves (FORC) Diagrams of Co Nanowire Arrays.* Journal of Nanoscience and Nanotechnology, 2008. **8**(11): p. 5725-5732.
68. Peixoto, T.R.F. and D.R. Cornejo, *Characterizing magnetic interactions in Ni nanowires by FORC analysis.* Journal of Magnetism and Magnetic Materials, 2008. **320**(14): p. E279-E282.
69. Katzgraber, H.G., et al., *Reversal-Field Memory in the Hysteresis of Spin Glasses.* Physical Review Letters, 2002. **89**(25): p. 257202.
70. Chen, D.X., J.A. Brug, and R.B. Goldfarb, *Demagnetizing factors for cylinders.* Magnetics, IEEE Transactions on, 1991. **27**(4): p. 3601-3619.
71. Ferré, R., et al., *Magnetization processes in nickel and cobalt electrodeposited nanowires.* Physical Review B, 1997. **56**(21): p. 14066-14075.
72. Skomski, R., et al., *Magnetic localization in transition-metal nanowires.* Physical Review B, 2000. **62**(6): p. 3900-3904.
73. Sun, L., et al., *Tuning the properties of magnetic nanowires.* IBM Journal of Research and Development, 2005. **49**(1): p. 79-102.
74. Zheng, M., et al., *Magnetic properties of Ni nanowires in self-assembled arrays.* Physical Review B, 2000. **62**(18): p. 12282-12286.
75. Parkin, S.S.P., *Systematic Variation of the Strength and Oscillation Period of Indirect Magnetic Exchange Coupling through the 3d, 4d, and 5d Transition-Metals.* Physical Review Letters, 1991. **67**(25): p. 3598-3601.
76. Parkin, S.S.P., R. Bhadra, and K.P. Roche, *Oscillatory Magnetic Exchange Coupling through Thin Copper Layers.* Physical Review Letters, 1991. **66**(16): p. 2152-2155.
77. Hashimoto, A., et al., *Marked enhancement of synthetic-antiferromagnetic coupling in subnanocrystalline FeCoB/Ru/FeCoB sputtered films.* Applied Physics Letters, 2006. **89**(3).
78. Jung, H.S., et al., *Magnetic domain-free hard-magnet-biased soft magnetic underlayers for perpendicular media.* Journal of Applied Physics, 2006. **99**(8).
79. Guedes, A., et al., *Study of synthetic ferrimagnet-synthetic antiferromagnet structures for magnetic sensor application.* Journal of Applied Physics, 2006. **99**(8).
80. Radu, C., et al., *Reversible susceptibility studies of magnetization switching in FeCoB synthetic antiferromagnets.* Journal of Applied Physics, 2007. **101**(9).
81. Spinu, L., et al., *Vectorial mapping of exchange anisotropy in IrMn/FeCo multilayers using the reversible susceptibility tensor.* Physical Review B, 2003. **68**(22).
82. Lee, Y.J., et al., *Theoretical studies of oscillatory behavior for long-range exchange bias.* Journal of Magnetism and Magnetic Materials, 2002. **239**(1-3): p. 57-59.
83. Lee, Y.J., et al., *Long-range exchange bias through a metal spacer.* Journal of Magnetism and Magnetic Materials, 2002. **240**(1-3): p. 264-266.
84. Pike, C.R., *First-order reversal-curve diagrams and reversible magnetization.* Physical Review B, 2003. **68**(10).
85. Pike, C.R., et al., *First-order reversal curve diagram analysis of a perpendicular nickel nanopillar array.* Physical Review B, 2005. **71**(13).
86. Beron, F., D. Menard, and A. Yelon, *First-order reversal curve diagrams of magnetic entities with mean interaction field: A physical analysis perspective.* Journal of Applied Physics, 2008. **103**(7).
87. Junginger, F., et al., *Quantitative determination of vortex core dimensions in head-to-head domain walls using off-axis electron holography.* Applied Physics Letters, 2008. **92**(11).
88. Katzgraber, H.G., et al., *Reversal-field memory in magnetic hysteresis.* Journal of Applied Physics, 2003. **93**(10): p. 6617-6619.

Vita

The author was born in New Orleans, Louisiana in 1982. Never attending high school, he went on to obtain his Bachelor of Science degree in physics from the University of New Orleans in 2010. During his time as an undergraduate he became a member of Professor Leonard Spinu's research group. He joined the University of New Orleans physics graduate program in 2010 to pursue a Masters in applied physics where he continued to perform research in Professor Leonard Spinu's research group.